Cell Reports

Article

KS10076, a chelator for redox-active metal ions, induces ROS-mediated STAT3 degradation in autophagic cell death and eliminates ALDH1$^+$ stem cells

Graphical abstract

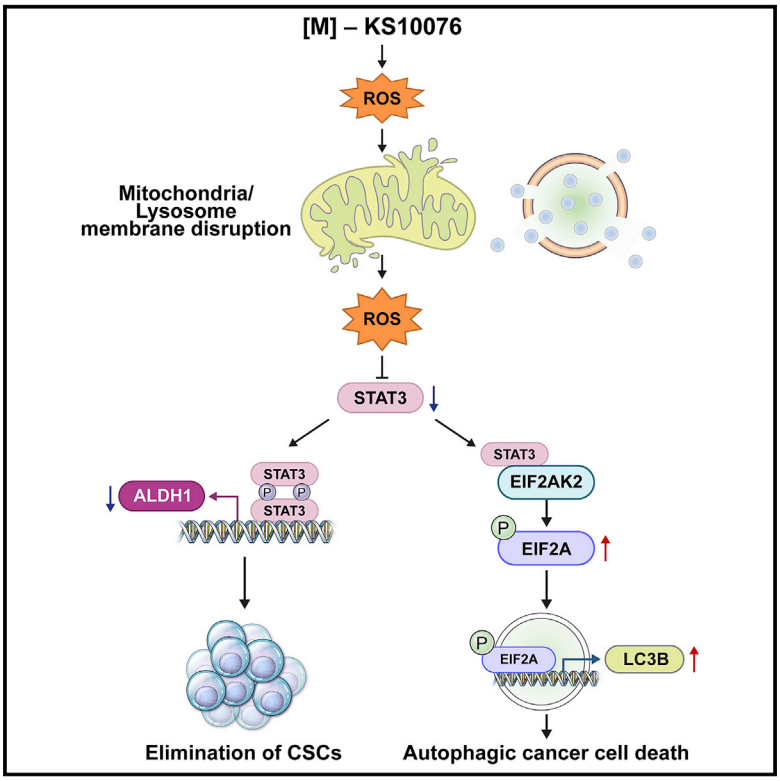

Highlights

- Drug screening identifies a metal chelator, KS10076, with potent cytotoxicity
- KS10076 destabilizes STAT3 by elevating ROS
- ROS-mediated STAT3 degradation affects mitochondrial and lysosomal membrane disruption
- KS10076 induces autophagic cell death and eliminates ALDH1+ cancer stem cells

Authors

Jaehee Kim, Areum Park, Jieon Hwang, ..., Uyeong Choi, Hyuk Lee, Sang Joon Shin

Correspondence

leeh@krict.re.kr (H.L.),
ssj338@yuhs.ac (S.J.S.)

In brief

Kim et al. report that a metal chelator, KS10076, increases intracellular ROS and degrades STAT3 in cancer cells. Elevation of ROS by KS10076 leads to organelle dysfunction and removes cancer stem cells, resulting in autophagic cancer cell death in both *in vitro* and *in vivo* models.

Kim et al., 2022, Cell Reports *40*, 111077
July 19, 2022
https://doi.org/10.1016/j.celrep.2022.111077

CellPress

Cell Reports

CellPress
OPEN ACCESS

Article

KS10076, a chelator for redox-active metal ions, induces ROS-mediated STAT3 degradation in autophagic cell death and eliminates ALDH1$^+$ stem cells

Jaehee Kim,[1,2,11] Areum Park,[3,4,11] Jieon Hwang,[1,2,11] Xianghua Zhao,[2] Jaesung Kwak,[3] Hyun Woo Kim,[5] Minhee Ku,[6,7] Jaemoon Yang,[6,7] Tae Il Kim,[8] Kyu-Sung Jeong,[4] Uyeong Choi,[1,2] Hyuk Lee,[3,9,*] and Sang Joon Shin[1,2,10,12,*]

[1]Department of Medicine, Yonsei University College of Medicine, Seoul 03722, Republic of Korea
[2]Songdang Institute for Cancer Research, Yonsei University College of Medicine, Seoul 03722, Republic of Korea
[3]Infectious Diseases Therapeutic Research Center, Korea Research Institute of Chemical Technology, Daejeon 34114, Republic of Korea
[4]Department of Chemistry, Yonsei University, Seoul 03722, Republic of Korea
[5]Chemical Data-Driven Research Center, Korea Research Institute of Chemical Technology (KRICT), Daejeon 34114, Republic of Korea
[6]Department of Radiology, Yonsei University College of Medicine, Seoul 03722, Republic of Korea
[7]Severance of Radiology, Yonsei University College of Medicine, Seoul 03722, Republic of Korea
[8]Division of Gastroenterology, Department of Internal Medicine, Yonsei University College of Medicine, Seoul 03722, Republic of Korea
[9]Graduate School of New Drug Discovery and Development, Chungnam National University, Daejeon 34134, Republic of Korea
[10]Division of Medical Oncology, Department of Internal Medicine, Yonsei Cancer Center, Yonsei University College of Medicine, Seoul 03722, Republic of Korea
[11]These authors contributed equally
[12]Lead contact
*Correspondence: leeh@krict.re.kr (H.L.), ssj338@yuhs.ac (S.J.S.)
https://doi.org/10.1016/j.celrep.2022.111077

SUMMARY

Redox-active metal ions are pivotal for rapid metabolism, proliferation, and aggression across cancer types, and this presents metal chelation as an attractive cancer cell-targeting strategy. Here, we identify a metal chelator, KS10076, as a potent anti-cancer drug candidate. A metal-bound KS10076 complex with redox potential for generating hydrogen peroxide and superoxide anions induces intracellular reactive oxygen species (ROS). The elevation of ROS by KS10076 promotes the destabilization of signal transducer and activator of transcription 3, removes aldehyde dehydrogenase isoform 1-positive cancer stem cells, and subsequently induces autophagic cell death. Bioinformatic analysis of KS10076 susceptibility in pan-cancer cells shows that KS10076 potentially targets cancer cells with increased mitochondrial function. Furthermore, patient-derived organoid models demonstrate that KS10076 efficiently represses cancer cells with active KRAS, and fluorouracil resistance, which suggests clinical advantages.

INTRODUCTION

Iron is an essential mineral that serves as a prosthetic group for various proteins involved in numerous cellular processes (Torti and Torti, 2013). As an enzyme cofactor, iron is necessary for DNA synthesis and mitochondrial metabolism. Accordingly, iron homeostasis is tightly regulated in normal physiology, coordinating efficient acquisition, storage, transportation, and recycling of iron. As iron is deeply involved in cellular proliferation, cancer cells exploit iron accumulation to support their aberrant growth and metabolism (Torti et al., 2018). Thus, iron addiction is a hallmark of cancers.

In mitochondria, redox-active transition metals, including iron, assist electron transport chain (ETC) cycling by partnering with oxygen-carrying proteins to deliver electrons; iron forms the Fe-S cluster in the ETC complex I (NADH dehydrogenase), complex II (succinate dehydrogenase), complex III (cytochrome *c* oxido-reductase) while copper participates in reducing oxygen to water in complex IV (cytochrome *c* oxidase) (Basu et al., 2013; Xu et al., 2013). Each stage of the ETC functions as a mitochondrial hub to fuel swift metabolism in aggressive cancers; NADH/NAD^+ for glycolysis and pyruvate dehydrogenase transition to acetyl CoA, fumarate from succinate for TCA cycling, $FADH_2$/FAD for fatty acid β-oxidation (Martínez-Reyes and Chandel, 2020; Zong et al., 2016). Alternatively, the blockade of ETC activity results in electron leakage, loss of mitochondrial membrane potential, and, eventually, mitochondrial damage. Therefore, transition metal ions are essential in maintaining mitochondria, especially in cancer cells with higher dependency on mitochondrial functions. Correspondingly, transition metal irons variably affect cellular metabolism reprogramming and reactive oxygen species (ROS) regulation in high-grade cancers (Schöpf et al., 2020; Valcarcel-Jimenez et al., 2017).

ROS is mainly generated from ETC; electrons leaked from complex I and III convert abundant oxygen molecules in the mitochondria into superoxide anions, which are subsequently

dismutated into hydrogen peroxides (Raimondi et al., 2020; Turrens, 2003; Zhao et al., 2019). These ROS are cleared by CATs, GPXs, SODs, and other antioxidants; uncontrolled ROS can destroy organelles, induce posttranslational modifications in oxidation-sensitive proteins, and promote multiple types of cell death (Kirkman and Gaetani, 1984; Palde and Carroll, 2015). To survive and benefit from ROS produced by increased oxidative phosphorylation (OXPHOS), high-grade cancers with swift metabolism upregulate their antioxidant and scavenging pathways against ROS-mediated cellular damage. One antioxidant pathway involves the enrichment of the NADPH pool. In the presence of abundant transition metals, aggressive cancer cells with active mitochondria support NADPH pools via enzymatic activities of various mediators: nicotinamide nucleotide transhydrogenase in mitochondrial inner membranes, isocitrate dehydrogenase (IDH) in α-ketoglutarate-mediated TCA cycle, G6PD in the pentose phosphate pathway, aldehyde dehydrogenase 1 (ALDH1) in folate-mediated one-carbon metabolism, and carnitine palmitoyltransferase-mediated fatty acid oxidation (FAO) (Ju et al., 2020; Moreno-Sánchez et al., 2017). The enriched NADPH is then used as an electron-transfer partner for antioxidant activities to enhance drug resistance and stemness in cancers. Besides, aggressive cancer cells with high ROS also upregulate unfolded protein response (UPR) and autophagy-lysosomal pathway clearing signaling to remove damaged cellular components, thus preventing their toxicity accumulation, which threatens cancer cell survival (Jung et al., 2014; Jang, 2018).

Regarding the complex interrelation between metabolism and ROS homeostasis in cancer cells, transition metals play dual roles, either to generate or regulate ROS mainly by assisting mitochondrial functions. Besides, copper, zinc, and manganese also serve as essential cofactors of the antioxidant enzyme superoxide dismutase family (SOD1 and SOD2, respectively) in the mitochondrial inner membrane and matrix to maintain homeostasis of the elevated ROS in cancer cells (Griess et al., 2017; Xu et al., 2013). Therefore, interrupting metal homeostasis in cancer is an attractive target mechanism for suppressing cancer cell respiration and proliferation, ROS regulation, and cancer cell stemness.

The dysregulation of metal homeostasis in cancer cells has led to the development of metal chelators as anti-cancer agents to sequester essential elements (Merlot et al., 2013). Metal chelators are either naturally derived from microbial sources or synthesized chemical process. Traditionally, metal chelators have been used to treat toxicities associated with accumulation and overload of metals, including iron (Crisponi et al., 2019). Recently, this class of drugs have been truly recognized for their use as anti-cancer drugs. Siderophores, such as deferoxamine, are chelators generated from microorganism (Keberle, 1964) and have been used to treat hepatocellular carcinoma (Yamasaki et al., 2011). Synthetic iron chelators, such as triapine, Dp44mT, COTI-2, and deferasirox, possess improved pharmacokinetic (PK) properties over the older-generation chelators (Ibrahim and O'Sullivan, 2020; Salim et al., 2016; Shakya and Yadav, 2020; Kalinowski et al., 2009). Unlike traditional metal chelators promoting the coordination and excretion of metals from the body, new synthetic chelators can sequester metals and become trapped within the lysosome of cancer cells, generating ROS and ultimately inducing cytotoxicity (Lovejoy et al., 2011). It was noteworthy that the treatment of chelators, including COTI-2 and NSC-319726, induced p53-dependent apoptosis (Lindemann et al., 2019; Yu et al., 2012). Also the further investigation revealed that the resistance mechanism of COTI-2 is related with ABCC1-mediated efflux (Bormio Nunes et al., 2020). Although metal chelators share an overlapping mechanism of action (MoA), different PK and pharmacodynamics properties can be exploited to combat the heterogeneous nature of cancers, highlighting the need to synthesize and screen diverse candidates.

In this study, we identified a metal-chelator and demonstrate a drug susceptibility-based genetic profiling strategy for integrated understanding of the MoA of a metal-trafficking drug. Moreover, we validated its efficacy using various model systems focusing on modes of cell death and target populations.

RESULTS

Identification and characterization of a metal chelator with anti-cancer effect

To target transient metal-dependency in pan-cancers, we synthesized more than 80 thiosemicarbazone compounds featuring thiazole groups as a nitrogen donor instead of the pyridyl group of previously reported di-2-pyridylketone thiosemicarbazone derivatives (Richardson et al., 2006; Kalinowski et al., 2007; Bernhardt et al., 2009). Among these, KS10031 showed remarkable cytotoxic efficacy in 100 cancer cell lines of different types; 92 cell lines exhibited nanomolar sensitivity (half-maximal inhibitory concentration [IC_{50}] < 1 μM), 7 had acceptable susceptibility (1 μM $\leq$ IC_{50} < 5 μM), and only Caki-2 showed insensitivity (IC_{50} = 67 μM) against KS10031 (Table S1). After optimization, KS10076 was identified to exert comparable cytotoxicity on cancer cells with far superior PKs than KS10031 (Figure 1C; Table S2). Notably, KS10076 showed great absorption and long half-life *in vivo* (C_{max} = 5.12 μg/mL and $T_{1/2}$ = 46.1 h) when orally administered, exceeding those of KS10031 and even DpC (iron-chelator in phase I trials). KS10076 also exceeded DpC with a lower plasma binding and an improved plasma stability in human, mice, and rat serums, thereby indicating better PK values (Figures 1C; Table S2).

A series of DpT and DpC derivatives were known to form 1:2 (metal/ligand) complexes with biologically abundant transition metal ions (Jansson et al., 2010; Lovejoy et al., 2012; Stacy et al., 2016). To identify the chelating mode of KS10076 to transition metal ions, we synthesized 1:2 complexes using Fe, Cu, and Zn precursors. While we could not obtain crystals of Fe and Cu complexes suitable for single-crystal X-ray analysis, the crystal of neutral 1:2 Zn(II)-KS10076 complex, [Zn(KS10076)$_2$], was obtained in dichloromethane/acetonitrile solution. The structure of [Zn(KS10076)$_2$] revealed that tridentate binding mode of KS10076 was identical with DpT or DpC derivatives where the NNS atoms coordinated to the metal center (Figure 1D). Interestingly, the one of KS10076 in the Zn complex was more strongly bound to Zn, resulting in significant distortion of another bound KS10076 (Figure S1A). This structural

A

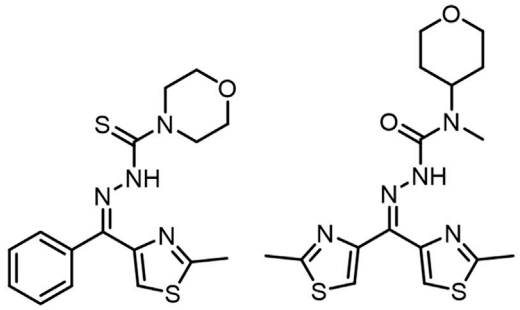

B

	Cell lines	Lineage	IC_{50} (μM)	
			KS10031	KS10076
Sensitive	PFEIFFER	Lymphoma	0.038	0.002
	HCT116	Colorectal	0.012	0.008
	KARPAS299	Lymphoma	0.021	0.015
	COLO205	Colorectal	0.045	0.025
	SW480	Colorectal	0.094	0.055
Less-sensitive	CAKI1	Kidney	0.060	0.056
	LS1034	Colorectal	0.091	0.070
	COLO201	Colorectal	1.582	1.382
	EFM192A	Breast	1.289	1.506
	SNUC1	Colorectal	3.991	1.836
Insensitive	CAKI2	Kidney	48.23	10.03

C

	KS10076	
PK parameters	I.V.	P.O.
T_{max} (h)	0.083 ± 0.000	0.400 ± 0.335
C_{max} (μg/mL)	8.720 ± 5.218	5.122 ± 2.859
$T_{1/2}$ (h)	22.29 ± 9.287	46.11 ± 17.52
$AUC_{0\text{-}8\ hr}$ (μg·h/mL)	58.06 ± 9.659	86.94 ± 17.52
AUC_{inf} (μg·h/mL)	72.38 ± 8.527	171.1 ± 74.56
CL (mL/h/kg)	27.88 ± 3.152	
V_{ss} (mL/kg)	785.7 ± 374.3	

	Species	KS10076
Plasma protein binding rate (%)	Mouse	99.86 ± 0.02
	Rat	95.12 ± 4.48
	Human	98.80 ± 0.34
Plasma stability (%)	Mouse	84.69 ± 7.44
	Rat	73.27 ± 2.01
	Human	76.08 ± 5.09

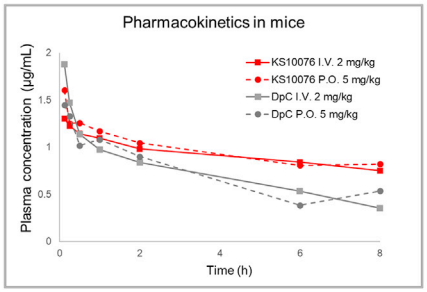

D

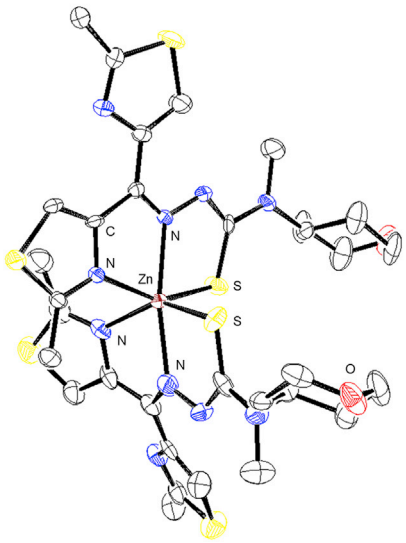

Figure 1. Identification and evaluation of metal chelators as anti-cancer candidates

(A) The structure of KS10031 and KS10076.

(B) Cytotoxicity (IC_{50}) of KS10031 and KS10076 in 11 cell lines of different cancer types. Compounds (0.001–3 μM) were treated for 48 h and the growth inhibitory rates were measured using the CCK-8 cell viability kit.

(C) Top: pharmacokinetic parameters were measured after administration of KS10031 and KS10076 (i.v. at 2 mg/kg and p.o. at 5 mg/kg, n = 4). See also Figure S1B. Middle: plasma protein binding and plasma stability (percentage remaining after 4 h incubation at 37°C) in mouse, rat, and human serum was measured (n = 3). See also Table S2. Bottom: pharmacokinetics graph of DpC and KS10076 (i.v. at 2 mg/kg and p.o. at 5 mg/kg, n = 4).

(D) Molecular crystal structure of $[Zn(KS10076)_2]$.

asymmetry highlights a unique five-membered thiazole donor group in KS10076 instead of a six-membered pyridyl group in DpT or DpC series. To determine the binding partners of KS10076, we tested different metal ions found inside human cells using the density functional theory, which predicts the binding energy through quantum modeling. The results showed that KS10076 readily interacts with iron, copper, manganese, and zinc (−ΔE = 75–175 kcal/mol; Figure S1B).

Next, we synthesized and measured the redox potential of 1:2 metal-KS10076 complexes, $[Fe(KS10076)_2]PF_6$ and $[Cu(KS10076)_2]$, using cyclic voltammetry (Figures S2A and S2B). The copper complex afforded Cu(I/II) redox potential at −1.15 V versus $F_C^{0/+}$, and the iron complex exhibited Fe(II/III) redox potential at −0.59 V versus $F_C^{0/+}$. These observed redox potentials were comparable with previously reported bis-ligated thiosemicarbazone metal complexes, implying that KS10076 has a similar mechanism to the thiosemicarbazone metal chelator compounds on cancer cells (Stefani et al., 2013).

Genetic profiling by KS10076 susceptibility depicts phenotypic features to understand drug MoA

To investigate the MoA of KS10076, we performed RNA sequencing (RNA-seq) analysis in six cell lines. In principal-component analysis (PCA), the direction from control to the treatment group was consistent in both (PC1 and PC2) axis across all cell lines, except CAKI2, which exhibited the exact opposite direction on both axes (Figure 2A). This implies that the components in PC1 and PC2 explain the cellular response to KS10076, either by sensitization or by providing protection. Besides, the distances moved by the arrows in sensitive cell lines (HCT116 and COLO205) on PC1 axis are farther than those of relatively less-sensitive cell lines (EFM192A).

Next, we identified the networks of the gene sets from the differentially expressed genes after KS10076 treatment (Figure 2B) to have comprehensive insight on KS10076 effect. First, gene sets of metal homeostasis were upregulated after treatment, showing that KS10076 disrupts metal regulation and usage in cellular contexts. Second, KS10076 downregulated gene sets required for increased proliferation in cancer cells, including those for the cell cycle (S and G2/M), PLK1-mediated proliferation, DNA repair, amino acid metabolism, and organelle biogenesis. Moreover, KS10076 upregulated genes in the cellular response to oxidative stress. Interestingly, the genetic response to oxidized phospholipids comprised genes that remove unfolded proteins (UPR) against excess ROS that disrupts proper protein folding or promotes abnormal protein postmodifications in cancers (Gargalovic et al., 2006; Jang, 2018).

Most notably, the gene sets related to mitochondrial functions were downregulated after KS10076 treatment. TCA cycle genes (especially, those that convert citrate from acetyl-CoA condensation as the first step of TCA cycle) were repressed across tested pan-cancer cell lines. Moreover, the genes involved in the ETC and OXPHOS systems (especially in complex I where NADH/NAD conversion by Fe-S coupling occurs) were repressed by KS10076. Moreover, KS10076 affected the synthesis, metabolism, and oxidation of fatty acids occurring in the mitochondria. FAO produces citric acid to fuel TCA cycle in cancer stem cells for the simultaneous utilization of fatty acid as an energy source and regenerating of NADPH for ROS regulation. Altogether, KS10076 interrupted metal homeostasis, cancer cell proliferation, ROS regulation, and mitochondrial functions.

To analyze the contributing features that determine drug susceptibility, we also profiled the basal gene expression of pan-cancer cell lines based on its sensitivity to KS10076. For comparative analysis, we assigned six cell lines with $IC_{50} < 1$ μM as "KS10076-sensitive cell lines" (PFEIFFER, HCT116, KARPAS299, SW480, CAKI1, and LS1034) and four cell lines with $IC_{50} \geq 1$ μM as "KS10076-less-sensitive cell lines" (COLO201, SNUC1, EFM192A, and CAKI2), and conducted a gene set enrichment analysis of KS10076-sensitive cell lines versus KS10076-insensitive cell lines and vice versa.

KS10076-sensitive cell lines were enriched with the IL6/JAK/STAT3 oncogenic signaling pathway, the epithelial-mesenchymal transition (EMT) pathway, active KRAS signaling, and MYC target genes (Figures 2C and 2D). STAT3, EMT, and KRAS are oncogenic and prognostic markers for aggressive cancers, and are the main causes of therapeutic failure in conventional chemotherapy due to development of drug resistance and cancer cell stemness. Interestingly, the "leading genes" (genes that strongly affect/influence a geneset enrichment scoring) of KRAS signaling enrichment in KS10076-sensitive cell lines showed significantly higher expression of *ETS1* (ETS proto-oncogene1), *LAPTM5* (lysosomal protein transmembrane 5), *CTSS* (cathepsin S), and *ATG10* (autophagy-related 10) genes, which participate in clearing damaged proteins and lipids from cancer cells with elevated ROS via lysosomal trafficking and autophagy (Table S3). Moreover, the leading genes of MYC target signaling also contained proteasome genes required for UPR (Figure 2D), supporting the recent reports that autophagy can be therapeutically targeted in cancers harboring KRAS mutation (Bryant et al., 2019; Kinsey et al., 2019). *PSMA1*, *PSMA2*, *PSMA4*, and *PSMB2* (proteasome 20S subunits), *PSMC6*, *PSMD1*, *PSMD7*, and *PSMD14* (proteasome 26S subunits), and *UBE2E1* (ubiquitin conjugating enzyme) were highly expressed in KS10076-sensitive cell lines, while KS10076-less-sensitive cell lines had low expression of these genes. Altogether, the results suggest that overexpression of autophagy and proteasome degradation system affect KS10076 sensitivity and that the higher efficacy of KS10076 in cancer cells with upregulated genes in these pathways provides insights into clinical implications.

Furthermore, while OXPHOS was enriched in KS10076-sensitive cell lines with no statistical significance, NADPH-related genes, including ubiquinone reductase subunits (*NDUFV2*, *NDUFS4*, *NDUA9*, and *NDUFAB1*), *UQCRC2* (ubiquinol-cytochrome *c* reductase core protein 2), and *COX7A2L* (cytochrome *c* oxidase subunit 7A2 like) were notably upregulated in KS10076-sensitive cell lines but not in KS10076-less-sensitive cell lines (Figures 2C and 2D; Table S3). These genes are essential for mitochondrial redox and electron cycling. Also, EIF2S2, eukaryotic translation initiation subunit 2, which is responsible for functional mitochondrial respiration (Raini et al., 2017), was highly expressed in KS10076-sensitive cells compared with less-sensitive cell lines, showing that KS10076-sensitive cell lines have enhanced demands for mitochondrial respiration and ETC functions, which are potent targets of KS10076 interruption.

In contrast, KS10076-less-sensitive cell lines were enriched with genes for glycolysis and adipogenesis. Upregulation of *HK2* (hexokinase 2), *G6PD* (glucose-6-phosphate dehydrogenase), and *PC* (pyruvate carboxylase) implies a metabolic shift toward enhanced glycolytic oxidation, or the Warburg effect, while the upregulation of *COPT* (carnitine palmitoyltransferase 2), *ETFB* (electron transfer flavoprotein subunit beta), *IDH1*

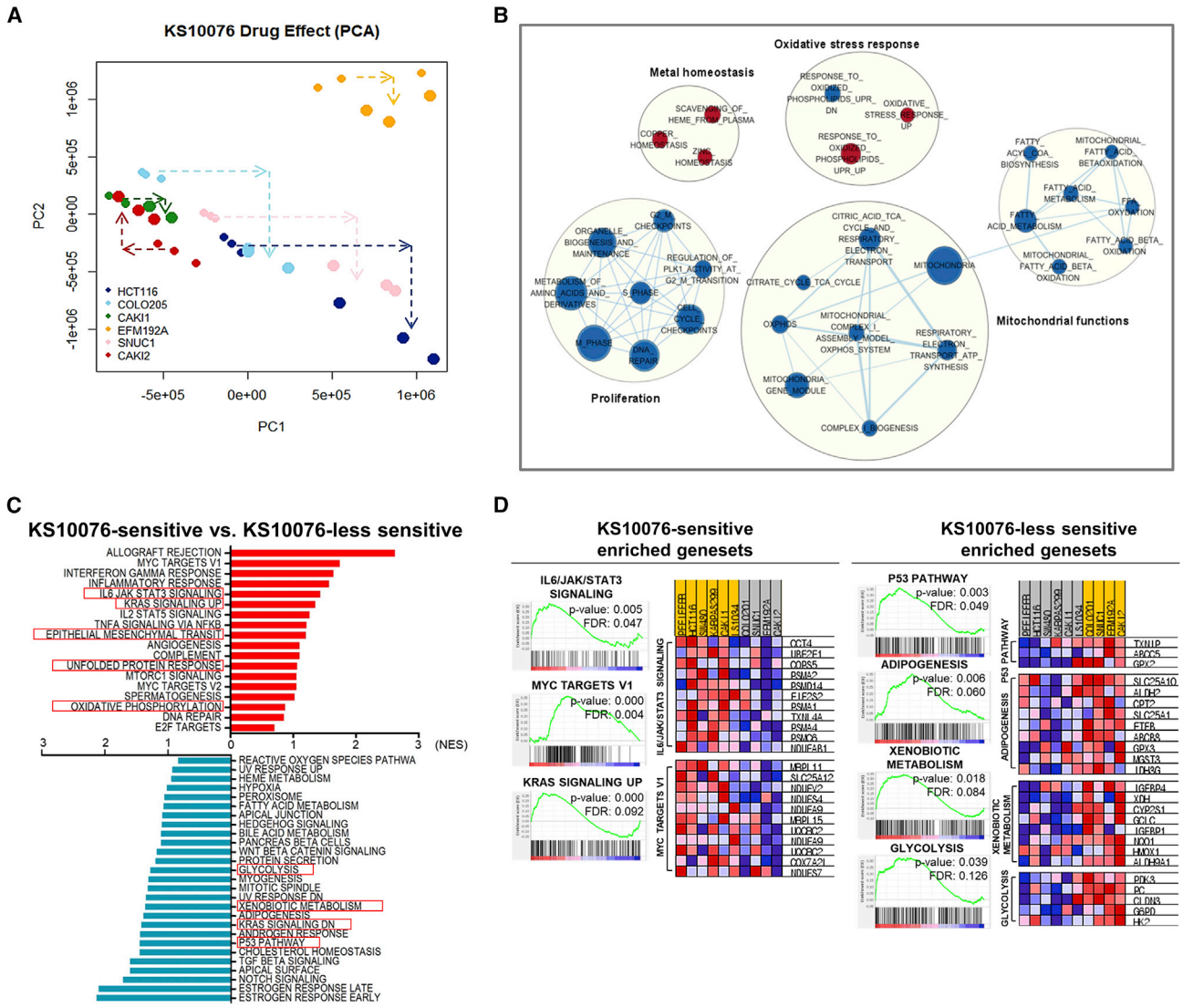

Figure 2. Genetic profiling of KS10076 drug response and susceptibility-determining factors

(A and B) RNA-seq was conducted using six cell lines treated with or without KS10076 at 1 μM for 24 h. Triplicates of each sample were independently used for analysis.

(C–D) Gene expression data from the CCLE portal were analyzed. Differentially expressed genes on KS10076-sensitive cell lines (PFEIFFER, HCT116, KARPAS299, SW480, CAKI1, and LS1034) versus KS10076-less-sensitive cell lines (COLO201, SNUC1, EFM192A, and CAKI2) were computed using gene set enrichment analysis (GSEA) software.

(A) Principal-component analysis of six cell lines' RNA-seq data. Controls are indicated by small circles and KS10076-treated samples as larger circles. The arrows indicate shifts from control to treatment groups.

(B) Geneset network analysis using GSEA and Cytoscape softwares on control versus KS10076.

(C) Genesets from GSEA analysis with |NES (normalized essential score)| > 1 are listed.

(D) Essentiality score plots with heat maps of selected leading genes are shown.

(isocitrate dehydrogenase 1), *ACO2* (aconitase 2), *ACOX1* (acyl-CoA oxidase 1), and *CS* (citrate synthase) demonstrates a shift toward fatty acid synthesis over other metabolic pathways. Among these, *G6PD*, *COPT*, and *IDH1* also act as the direct sources of NADPH production to support the enzymatic activity of antioxidants (Ju et al., 2020). Besides, KS10076-less-sensitive cell lines exhibited a significant upregulation of antioxidant genes in p53 pathways and xenobiotic metabolism. Upregulation of *GPX2* and *GPX3* (glutathione peroxidases to remove hydrogen peroxide), *GCLC*, the enzyme for glutathione synthesis, *OSGIN1* (oxidative stress induced growth inhibitor 1), *TXNIP* (thioredoxin interacting protein), *NQO1* (NADPH quinone dehydrogenase 1), and *HMOX1* (heme oxygenase) in KS10076-less-sensitive cell lines implies that enhanced antioxidant capacity can provide protection against KS10076. Accordingly, metabolic profiling of KS10076-sensitive and -less-sensitive

cell lines showed differential susceptibility to KS10076 in terms of mitochondrial function, OXPHOS, and glycolysis (Figure S3).

KS10076 exhibits cytotoxicity via direct involvement in redox activity

To examine the in-depth MoA of KS10076, we hypothesized that metal chelators can either deprive cells of essential transition metals or participate in the redox reactions to generate cytotoxic ROS. As shown in Figure S4A, we observed that KS10076 treatment decreased ferritin, while iron regulatory protein 2 increased in response to deprivation of labile irons (Cheng et al., 2014; Wang et al., 2020; Xiao et al., 2020). Moreover, the enzyme activity of the SOD family that requires metal cofactors, was repressed after KS10076 treatment (Figure S4B). To test whether the metal deprivation effect of KS10076 is the main cause of cell death, we tested cell viability using either $[Fe(KS10076)_2]PF_6$ or $[Cu(KS10076)_2]$. Interestingly, $[Cu(KS10076)_2]$ showed comparable cytotoxicity (IC_{50} = 5 nM) with KS10076 (IC_{50} = 4 nM), while $[Fe(KS10076)_2]PF_6$ had an IC_{50} value of 83 nM in HCT116 cells (Figure S4C). [M]-KS10076 complex ([M] = Fe or Cu) may substitute its metal partner after entering the cells, but it does not remove metal ions already present inside the cells. Therefore, the results show that KS10076 cytotoxicity is mediated mainly via [M]-KS10076 complex activity, rather than by depriving metal ions from the required activities to sustain survival.

As demonstrated earlier, [M]-KS10076 complexes are redox-active species; therefore, we conducted live cell imaging to examine whether the redox activity of [M]-KS10076 produces intracellular ROS (Figures 3A and 3B). In HCT116 cells, cellular ROS increased both time dependently and dose dependently while N-acetyl cysteine (NAC) co-treatment largely reversed the effect. Mitochondrial ROS became undetectable when cellular ROS was dispersed throughout the cells after 24 h treatment. Also, NAC addition had no substantial changes on the mitochondrial ROS. In SW480 cells, KS10076 at lower dose mainly increased the production of mitochondrial ROS, which was remarkably reversed by NAC addition. Also, KS10076 at higher concentration resulted in increased cellular ROS in SW480 cells, while NAC co-treatment retained the mitochondrial ROS. Similar changes were obtained by treatment with triapine, although deferoxamine minimally generated ROS (Figure S4D).

The mitochondrial ROS remained undetected after cellular ROS was dispersed throughout the HCT116 and SW480 cells, and therefore we investigated whether the organelle intactness is disturbed by live cell imaging (Figure 3C). The intensity and area of mitochondria-tracking fluorescence significantly decreased after KS10076 treatment, showing that the membrane potential of the mitochondria was disturbed by its disruption. Also, KS10076 reduced the fluorescence of the lysosomal tracker, demonstrating that the acidic pH of lysosomes is disrupted by membrane disruption after KS10076 treatment. Similar findings were obtained upon small interfering RNA (siRNA)-mediated downregulation of galectin-3 (Figure S4E), a key coordinator for lysosomal repair and removal (Jia et al., 2020a; 2020b). In addition, we found that galectin-3 transgenic cell line rescued KS10076-induced lysosomal disruption (Figure S4F). Furthermore, siRNA targeting lysosomal cathepsins, which are enclosed in the lysosomes that help to maintain the homeostasis of the cell's metabolism by participating in the degradation of autophagic material, partially rescued cytotoxicity of KS10076 (Figure S4G). Altogether, the results show that KS10076-induced ROS disrupts intracellular organelles that lead to the dispersion of cellular ROS.

Moreover, we examined whether the redox activity of [M]-KS10076 is responsible for its cytotoxicity in cancer cells. First, we assessed the growth inhibition activity of KS10076 with or without the presence of NAC, which is a precursor of reduced glutathione, an antioxidant. Remarkably, the antioxidant activity of NAC repressed the cytotoxicity of KS10076 in HCT116 (IC_{50} from 8 nM to 9 μM), SW480 (IC_{50} from 55 nM to 29 μM), and LS1034 (IC_{50} from 74 nM to 7 μM, Figures 3D and S4H) after a 48-h treatment session. Since the genetic profiling of KS10076 drug response affected ETC complexes and mitochondrial functions, we also assessed the effect of MitoQ, an antioxidant, against mitochondrial ROS. Unlike NAC, MitoQ alone was inadequate to insensitive cells against KS10076, but it still delayed the cytotoxic response in 24 h.

Finally, we monitored the ROS increase in seven pan-cancer cell lines with different susceptibilities against KS10076 (Figure 3E). Four KS10076-sensitive cell lines (HCT116, CAKI1, COLO205, and SW480 with IC_{50} < 60 nM) exhibited increases in both mitochondrial and intracellular ROS, whereas a less-sensitive cell, COLO201 (IC_{50} = 1 μM), showed only increased mitochondrial ROS that did not proceed to overall increase in intracellular ROS. Moreover, other cell lines that showed the least growth inhibition after KS10076 treatment (SNUC1 and CAKI2 with IC_{50} = 2 and 10 μM, respectively), showed no detectable increase in ROS. The results consistently demonstrate that KS10076 cytotoxicity depends on the redox potential of metal-bound complexes to generate excess ROS in different organelles, which proceeds to disrupt and damage the cells.

KS10076 induces STAT3 degradation and thereby promotes autophagic cell death via the EIF2A/LC3B signaling pathway

Based on our finding that gene enrichment on the STAT3 signaling pathway mediated KS10076 susceptibility, we examined if STAT3 is a potential KS10076 target. While none of the upstream kinases (SRC, JAK1, and c-Abl) and iron-mediated transducers in STAT3 stimulation (gp130 and CDK1) was consistently modulated upon KS10076 treatment in various cancer cell lines (data not shown), KS10076 consistently decreased pSTAT3 and total STAT3 protein but not the mRNA expression (Figure S5A). Next, we observed that the STAT3 stability was significantly destroyed after KS10076 treatment, while it was reversed by adding NAC (Figure 4A), showing that STAT3 degradation is ROS dependent. Moreover, KS10076 induced STAT3 ubiquitination, which was further accelerated by proteasome degradation, showed that KS10076-induced STAT3 ubiquitination is subject to proteasome degradation (Figure 4B).

Since STAT3 transcripts BCL2, an anti-apoptosis modulator, we performed time-course immunoblotting analysis (Figure 4C). While the expression of both STAT3 and pSTAT3 decreased remarkably after a 12 h KS10076 treatment, the expression of BCL2, an anti-apoptotic marker of the STAT3 target gene, remained unaffected. Alternatively, STAT3 degradation was

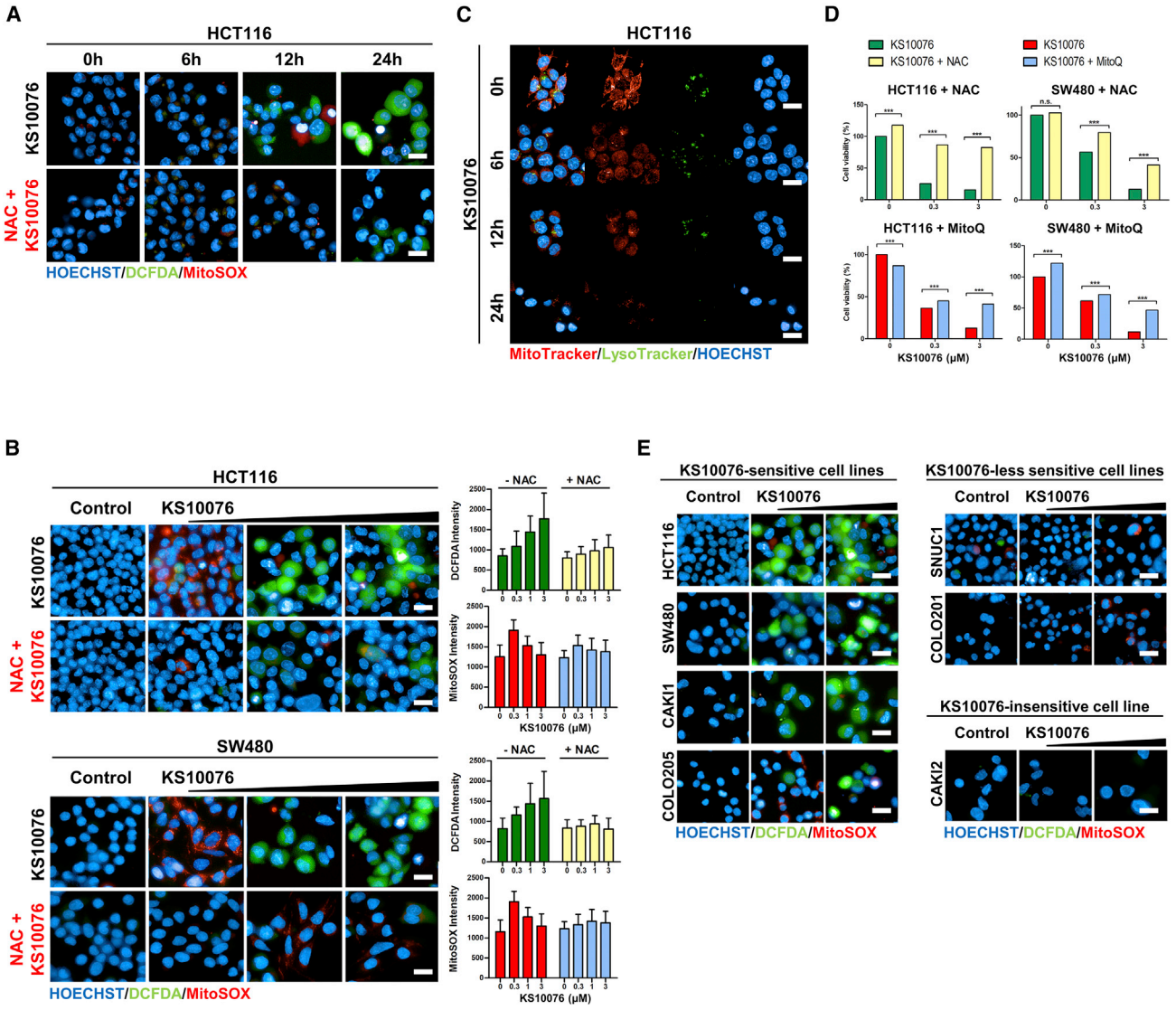

Figure 3. KS10076 induces cytotoxic ROS

(A–C) HCT116 and SW480 cells were treated with KS10076 with or without NAC and then subjected to live cell imaging using DCFDA (cellular ROS, green) and MitoSox (mitochondrial ROS, red) for ROS detection. The images were pictured at 20× magnification using Operetta CLS. The fluorescence intensity of each sample with three biological replications, each with six random fields was measured and quantified using Harmony software (number of nuclei per sample >200).

(A) HCT116 cells were treated with 3 μM of KS10076 for time course analysis.

(B) HCT116 and SW480 cells were treated with KS10076 (0, 0.03, 0.3, and 3 μM) for 24 h for analysis.

(C) HCT116 cells were treated with 3 μM of KS10076 for a time course analysis. Cells were fixed and stained for their mitochondria (MitoTracker, red) and lysosomes (LysoTracker, green).

(D) HCT116 and SW480 cells were treated with KS10076 and rescued by NAC co-treatment (5 mM) for 48 h. For MitoQ-rescued cells, the cells were treated with MitoQ (30 nM) after 6 h of KS10076 treatment and analyzed for 24 h.

(E) Pan-cancer cell lines were stimulated with KS10076 treatment (0, 1, and 3 μM) and ROS generation was observed by live cell imaging. Scale bars, 100 μm (A, B, C, and E). Data are presented as the mean ± SEM. ***$p < 0.005$.

followed by an abrupt increase in EIF2A phosphorylation and ATF4 and LC3B upregulation (both I and II). To regulate autophagy, the SH2 domain of cytoplasmic STAT3 mimics and competes with EIF2A to interact with EIF2AK2 at its catalytic site, thus hindering the phosphorylation at S51 of EIF2A (Harhous et al., 2019). Without STAT3, EIF2AK2 readily phosphorylates EIF2A, and the phosphorylated EIF2A in the nucleus activates transcription of ATF4, which subsequently transcripts essential autophagy markers, such as the ATG family and LC3B (B'Chir et al., 2013). To verify the hypothesis of KS10076 modulating autophagy via STAT3/EIF2AK2, a time-course immunofluorescence was conducted. As shown in Figure 4D, the control exhibited increased STAT3 molecule expression throughout the cells while EIF2A was retained only in the cytoplasm. When

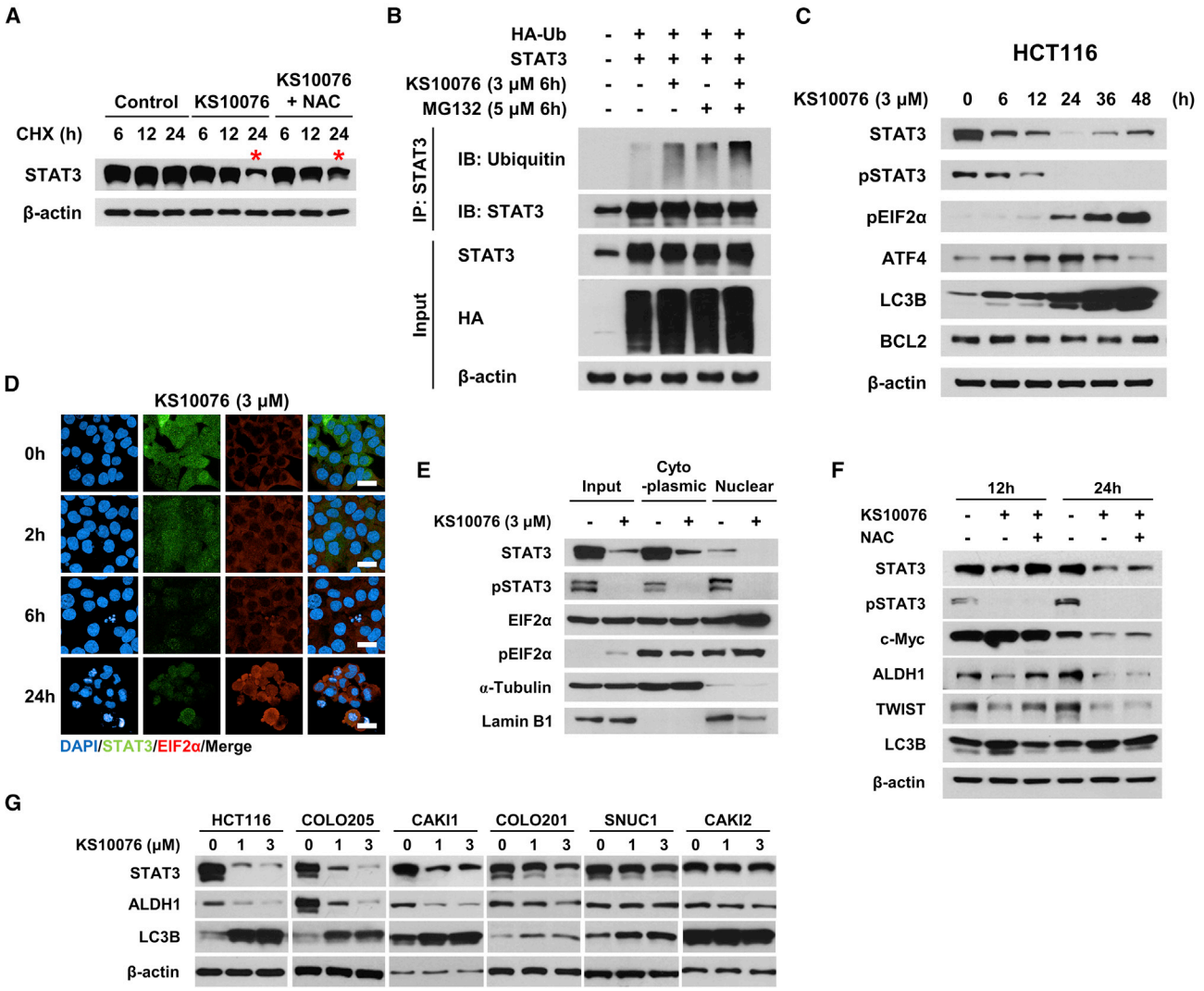

Figure 4. KS10076 destabilizes STAT3 and induces autophagy via EIF2A

(A) HCT116 cells were treated with KS10076 (3 μM) and cycloheximide (10 μg/mL) and harvested at different time points (t = 6, 12, and 24 h) for western blotting.

(B) HCT116 cells were transfected with HA-Ub and STAT3 expression plasmids for ubiquitination assay. After 24 h of transfection, cells were treated with KS10076 (3 μM) with or without MG132 (5 μM) for 6 h. Immunoprecipitates were subjected to immunoblotting using an anti-STAT3 antibody.

(C) HCT116 cells were treated with KS10076 (3 μM) for time-course analysis.

(D) HCT116 cells were treated with 3 μM of KS10076, fixed, and immunolabeled for confocal immunofluorescence imaging. Scale bars, 100 μm.

(E) HCT116 cells were treated with 3 μM of KS10076 and then fractionated for compartmental analysis.

(F) HCT116 cells were treated with 3 μM of KS10076 and NAC and subsequently subjected to immunoblotting to evaluate protein-rescuing effect by co-treatment of antioxidant.

(G) Pan-cancer cell lines (sensitive to insensitive from left to right) were treated with KS10076 for 24 h and then subjected to western blotting. See also Figure 1B.

KS10076 destabilized STAT3 (t = 6 h), EIF2A was translocated into the nucleus (t = 12–24 h). This change was accompanied with increased LC3B accumulation (Figure S5B). The nucleus-cytoplasmic fractionation and immunoblotting further confirmed that pSTAT3, STAT3, and cytoplasmic pEIF2A decreased while nuclear pEIF2A increased (Figure 4E), implying the translocation of pEIF2A following STAT3 degradation. Finally, we confirmed that the nuclear EIF2A increase was followed by the transcription of autophagy signaling genes, including *ATF4*, *ATG4B*, and *LC3B*, after KS10076 treatment in HCT116, LS1034, and COLO205 cells (Figure S5C). Similar findings were observed in the experiments with STAT3 inhibitors JSI-124 or Stattic (Figure S5D). To investigate the KS10076-induced autophagic cell death more strictly, we checked whether KS10076 induces typical changes of intracellular organelles through transmission electron microscopy (TEM). Findings from TEM also supported that KS10076 induces autophagic cell death based on increased formation of phagophores, autophagosomes, and autolysosomes (Figure S5E). This was further supported by the experiments revealing that siRNA-mediated knockdown of ATG7 or

EIF2A partially rescued KS10076-mediated cytotoxicity (Figure S5F). Furthermore, treatment with selective inhibitors of apoptosis (Z-VAD-FMK), ferroptosis (ferrostatin-1), necrosis (necrosulfonamide), and necroptosis (necrostatin-1) in addition to KS10076 revealed that autophagic cell death was the dominant pathway mediating cytotoxicity of KS10076 (Figure S5G).

Besides inducing autophagic cell death, KS10076 suppressed the expression of cell-proliferative (c-MYC and Ki67), pro-EMT (N-cadherin and Twist), and cancer stem cell markers (ALDH1, CD44, CD133, and CD44v6) in various cell lines (Figure S6A). Along with the changes, KS10076 treatment rearranged the HCT116 cell skeleton into a less protruding, round shape as demonstrated by F-actin staining, and the invasion ability was reduced (Figure S6B). Moreover, KS10076 treatment resulted in cell-cycle arrest at G_1/S not progressing into the M phase marked by Ki-67 and pHH3 (Figure S6C). Most importantly, KS10076 reduced key stem cell markers in 3D spheroids. ALDH1—an enzyme that detoxifies and self-protects against chemotherapy and maintains the CSC subpopulation (Martinez-Cruzado et al., 2016)—and CD44v6—which supports the stabilization of cysteine-glutamate exchanger and thereby enhances redox capacity and multidrug resistances (Ma et al., 2019)—were notably suppressed. Furthermore, KS10076 completely disaggregated the tumor spheres by one-time treatment, while DpC only reduced the size of the well-formed tumor spheres (Figure S6D).

Next, we wondered if the anti-cancer phenotypic changes were affected by ROS-mediated STAT3 maintenance. Indeed, c-MYC, ALDH1, and Twist were downregulated, while LC3B was upregulated by KS10076 treatment; however, the addition of NAC reversed it (Figure 4F). Moreover, the immunoblotting of various cancer cell lines showed that STAT3 degradation followed by ALDH1 and LC3B modulation was noticeable in KS10076-sensitive cell lines, but cell lines with less sensitivity to KS10076 showed lesser or no changes (Figure 4G). Degradation of p62 was evidently induced by KS10076 and reversed by chloroquine treatment (Figure S6E). Altogether, the results show that KS10076-mediated ROS destabilizes STAT3, which represses cancer stem cells, cell proliferation, and migration while inducing EIF2A/ATF4-mediated autophagic cell death across pan-cancer cell lines.

KS10076 eliminates pSTAT3/ALDH1+ stem cells in CRC patient-derived organoids

Genetic profiling based on drug-susceptibility also revealed that the upregulated genes during active KRAS signaling were enriched in the KS10076-sensitive group, while the downregulated genes during the same activity were enriched in the KS10076-less-sensitive group (Figure 5A). Therefore, we constructed 13 organoid models, which are derived from available clinical data of individual patients with colorectal cancer, including MSI status, KRAS/BRAF mutation profiles, cancer stages and progression, prognostics, and so on, and tested KS10076 cytotoxicity on the patient-derived organoids (PDOs) (Table S4). The overall efficacy of KS10076 ranged from IC_{50} values in the nM to μM range, which was comparable to the results from 2D screening, showing that KS10076 is equally effective in functionally assembled 3D models without penetrating issues. Similar to the gene analysis results, oncogenic KRAS mutations (G12D and G13D) were found in PDOs that were relatively more responsive to the treatment, whereas less-responsive organoids had wild-type KRAS (Figure 5A). Moreover, KS10076 effectively repressed the growth of YCO019, YCO013, and YCO016 organoids that were resistant against fluorouracil (5-FU), a conventional chemotherapy. These results suggest the clinical advantages of KS10076 in patients with poor outcomes due to resistance to conventional chemotherapeutics or active KRAS mutations.

Organoids form a miniature of the derived organs by allowing differentiation and self-organization of stem cells to achieve organ-specific cellular functions and structures. To test KS10076 suppression of cancer stemness, YCO013 PDOs were allowed to differentiate from the stem cells in the presence or absence of KS10076. The untreated YCO013 organoids formed a protruding bud from day 3 with high expression of nuclear pSTAT3 (shown as arrows in Figure 5D) and recapitulated the crypt-villus units with mucosa-like fluid inside the lumen of the enteroids on day 14 (Figure 5C). In contrast, KS10076 treatment blocked stem cell differentiation into a structured enteroid and dose dependently collapsed the morphology. To understand the role of STAT3 in organ-recapitulation of YCO013, YCO013 was subjected to immunostaining and results showed that YCO013 organoids coexpressed nuclear pSTAT3 in the central mass with high ALDH1 expressions on cellular membranes (Figures 5D and 5E). Moreover, pSTAT3 was highly expressed in the small bud protruding from its cystic body, suggesting that pSTAT3 is required for differentiation-aimed self-organization of stem cells. However, when KS10076 was treated, the expression of both pSTAT3 and ALDH1 were remarkably suppressed, showing that KS10076 eliminates pSTAT3/ALDH1+ stem cells. Decreased expression of ALDH1 protein was mainly driven by diminished transcription of ALDH1 (Figure S6F).

KS10076 suppresses tumor growth *in vivo* and eliminates STAT3 and ALDH1

Finally, we verified the tumor inhibitory effect of KS10076 *in vivo* by using HCT116 and SW480 murine xenograft models (Figures 6A–6C). KS10076 effectively inhibited tumor growth when orally administered at 8 mg/kg for 5 days/week compared with vehicle controls in HCT116 xenograft (Figure 6A). After a 24 day treatment period, the tumors started to regress, while a long-term treatment plan to test complete regression was impossible due to weight loss in the experimental groups (Figures S7A–S7B). The tumors were excised and subjected to immunoblotting within 6 h of the last administration. Consistent with the *in vitro* assays, KS10076 significantly reduced STAT3 and ALDH1 in HCT116 xenograft models compared with the vehicle controls (Figure 6D).

The murine xenograft of SW480 also showed more than 50% tumor growth inhibition when administered at a dose of 15 mg/kg daily for 3 days/week of KS10076 (Figure 6B). To avoid KS10076 toxicity accumulation, single or double administration per week was also tested (40 or 25 mg/kg, respectively). However, dosing schedules with >48 h time intervals revealed reduced therapeutic efficacy, since the half-life of KS10076 is about 46 h by administration. The tumors subjected to western blot showed STAT3 reduction proportional to the tumor volume and tumor weight

A

YCO Organoid	IC_{50} (μM)		Mutation
	KS10076	5-FU	KRAS
YCO019	0.015	129.5	KRAS G13D
YCO013	0.016	160.0	KRAS G13D
YCO016	0.017	160.0	KRAS G12D
YCO005	0.026	24.7	WT
YCO004	0.090	22.0	KRAS G12D
YCO011	0.178	19.3	KRAS G12D
YCO006	0.300	10.6	WT
YCO001	0.432	21.3	WT
YCO009	0.790	25.1	WT
YCO012	0.810	17.0	WT
YCO007	0.896	83.2	WT

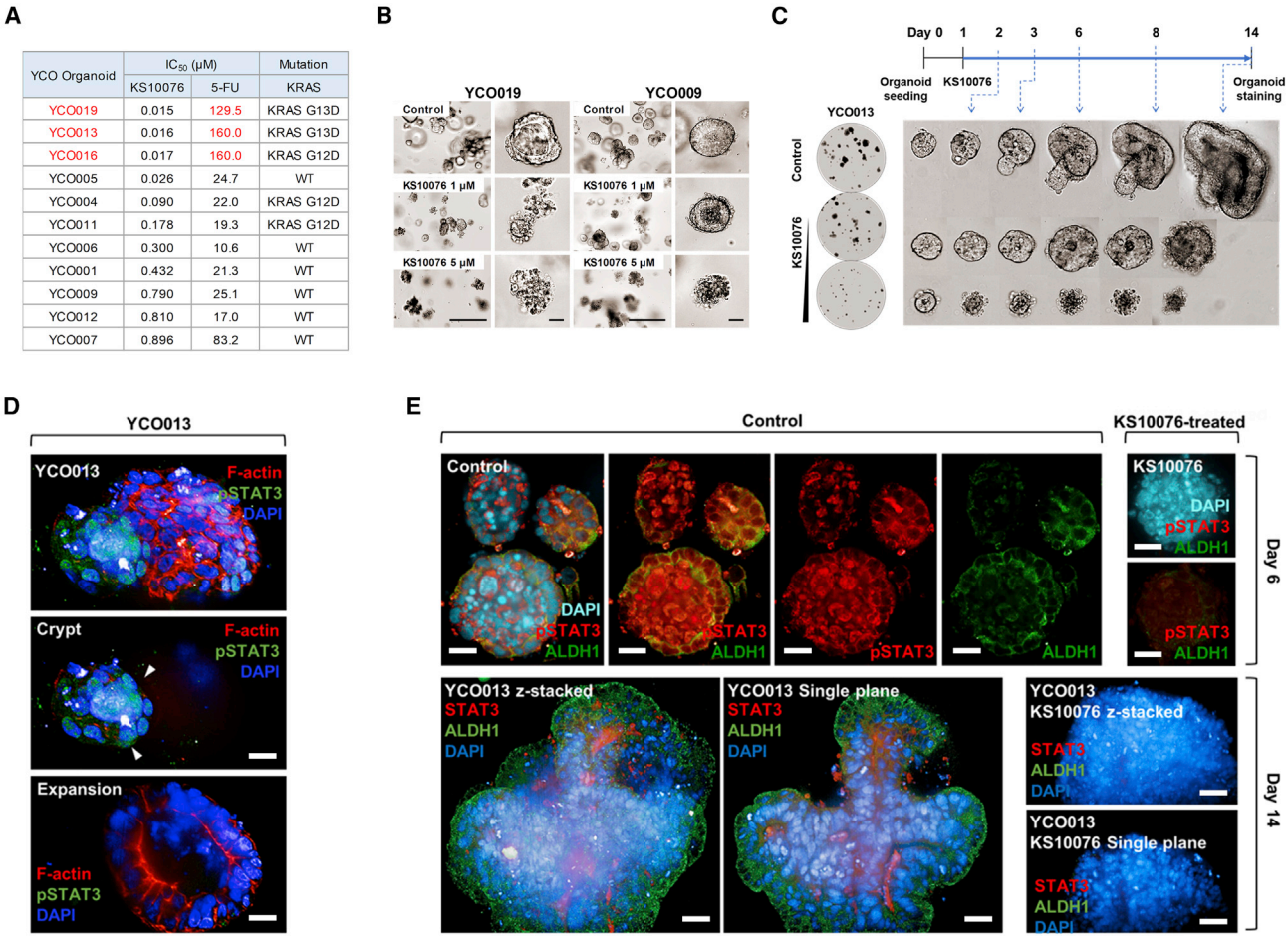

Figure 5. KS10076 eliminates cancer stem cells in tumor sphere and patient-derived organoid models

(A and B) Yonsei CRC patient-derived organoids (YCOs) were treated with KS10076 or 5-FU once for 5 days and subjected to cytotoxicity assay using CellTiter-Glo for quantification. Representative images were captured on day 5 using Operetta CLS at 5× and 20× magnification. Scale bars, 500 and 100 μm. See also Table S4.

(C–E) The CRC patient-derived YCO013 organoids were treated with KS10076 at 0, 10, and 100 nM in fresh medium every 4 days and tracked for 14 days. After 14 days, organoids were recovered from a 3D matrix and immunolabeled for confocal fluorescent analysis (20×).

across the dosing groups and vehicle controls (Figure 6E). Altogether, KS10076 showed therapeutic potential in repressing tumors and depleting STAT3/ALDH1 in tumors *in vivo*.

DISCUSSION

Cancer treatment strategies targeting metal homeostasis are intriguing, because metal modulation closely regulates metabolic switch, respiration, ROS capacity, and stemness in aggressive cancers. While there has been extensive research to evidence this, no therapeutic agent targeting metal homeostasis has been completely clarified. In this study, we report a chelator for redox-active metal ions with outstanding cancer inhibitory activity in pan-cancer cell lines, demonstrate the multi-aspects of its MoA, and indicate its clinical advantages along with important implications.

Firstly, our study takes a unique analytical approach to reveal a comprehensive understanding on metal chelation in pan-cancer cell lines. Screening of drug sensitivity on 100 cell lines followed by genetic profiling to compare enriched pathways between susceptible and less susceptible (or insensitive) cell lines allowed us to specify the MoA of KS10076. STAT3 signaling pathway was revealed as the drug target by the enriched pathways in the susceptible group, while the upregulation of proteasome degradation modulators revealed the mechanism of how KS10076-induced ROS affects STAT3 signaling. Moreover, the enrichment of genes for mitochondrial functions, including metabolism and respiration, indicated that KS10076 is effective in cells with high mitochondrial function demand as it is one of the key sources of KS10076-induced ROS. In contrast, the pathways enriched in less-sensitive groups reflect the resistance mechanism or are indicative of markers for non-responders. Enrichment of antioxidant genes, including GPX2, in a non-responsive group

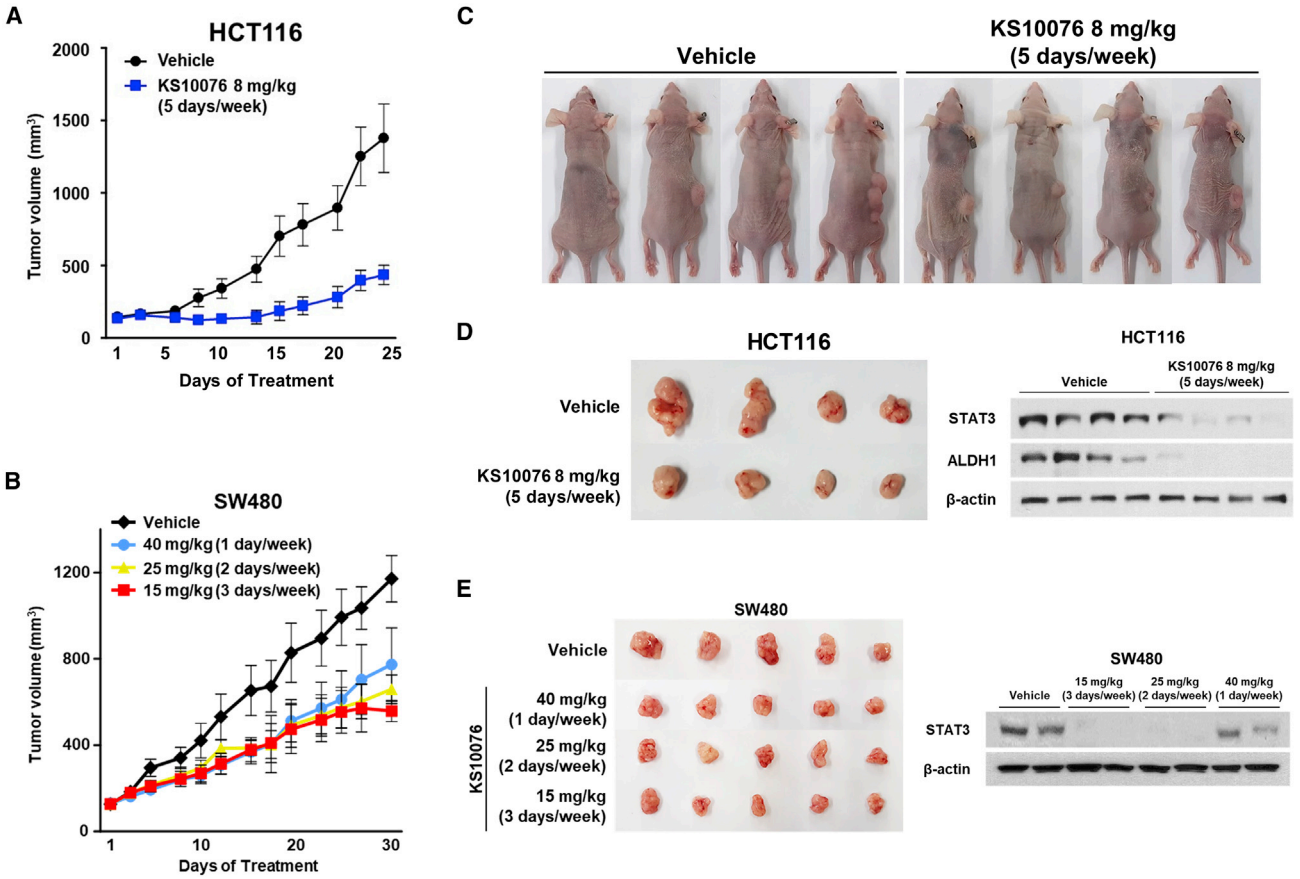

Figure 6. KS10076 represses tumor growth and eliminates STAT3/ALDH1+ cells *in vivo*

(A) HCT116 xenograft in BALB/c nude mice. Vehicle or KS10076 was orally administered as indicated (n = 4).

(B) SW480 xenograft in BALB/c nude mice. Vehicle or KS10076 was orally administered as indicated (n = 5).

(C) Representative image of HCT116 xenograft in BALB/c nude mice.

(D) Tumors from HCT116 xenograft in (A) were immunoblotted.

(E) Tumors from SW480 xenograft in (B) were immunoblotted. Data are represented as the mean ± SEM.

predicted that limiting ROS production in the first step of KS10076 MoA determines susceptibility. This analytical approach provided a multifaceted insight, which is required for drug discovery and development using metal chelators.

Secondly, drug screening on PDO models revealed clinical implications. KRAS-mediated metabolism and resistance against conventional first-line chemotherapy are intriguing but challenging subjects in oncology. In our study, KRAS signaling-mediated autophagic resistance mechanism against ROS was highlighted as a sensitizing factor against KS10076, while the original UPR is an essential factor for cancer cells to survive under metabolic stresses due to rapid proliferation and respiration. Here, we also demonstrate therapeutic strategy potential to target the interplay between UPR and stress response in KRAS-active cancers. Moreover, 5-FU-resistant cancer cells—comprising many stem cancer cells with tightly regulated ROS systems—were sensitized by the KS10076-mediated ROS. The mechanism behind overcoming chemoresistance by interrupting mitochondrial functions via excess ROS triggers should be further investigated with KS10076 and its metal chelator derivative, and this will provide a comprehensive insight to develop resistance-free therapeutic strategies.

Limitations of the study

Our study has some important limitations. Although we verified the therapeutic implication of KS10076 in a comprehensive manner, this agent exhibits a MoA that overlaps with other thiosemicarbazones, such as triapine, Dp44mT, and DpC (PMID: 31660812; PMID: 33190481; PMID: 21425997). Mechanistically, these agents commonly inhibit ribonucleotide reductase activity, resulting in ROS generation. Although we suggested that the results revealing comparable metal binding affinity between KS10076 and other compounds, a distinct MoA of KS10076 has not been studied in an extensive manner in this study except stability *in vivo*. In addition, there are also improvements needed for therapeutic success. The efficacy of KS10076 *in vivo* was clear when cytotoxicity appeared, showing the narrow therapeutic window within which it operates. The V_{ss} (volume of distribution at steady state) value under 1 L/kg in Figure 1C demonstrates that KS10076 has low tissue penetration ability. To

increase the delivery and penetration into tumor tissues, further studies on conjugation to other delivery systems are required; this may provide important solutions.

Besides, STAT3 postmodification and accelerating STAT3 degradation also require further investigation. While STAT3 has been recently reported to be oxidized upon ROS production via TRX1 and PRX1 antioxidant activities (Palde and Carroll, 2015; Sobotta et al., 2015), no evidence exists that this oxidization causes STAT3 destabilization and ubiquitin-dependent degradations. In line with this, the in-depth understanding on how the degradation of STAT3 is induced should be investigated in a delicate manner.

STAR★METHODS

Detailed methods are provided in the online version of this paper and include the following:

- KEY RESOURCES TABLE
- RESOURCE AVAILABILITY
  - Lead contact
  - Materials availability
  - Data and code availability
- EXPERIMENTAL MODEL AND SUBJECT DETAILS
  - Cell lines
  - Mice
- METHOD DETAILS
  - Synthesis of KS10031 and KS10076[a]
  - Synthesis of (2-methylthiazol-4-yl) (phenyl)methanol (2)
  - Synthesis of (2-methylthiazol-4-yl) (phenyl)methanone (3)
  - Synthesis of methyl hydrazinecarbodithioate (4)
  - Synthesis of methyl 2-((2-methylthiazol-4-yl) (phenyl) methylene)hydrazine-1-carbodithioate (5)
  - Synthesis of *N*'-((2-methylthiazol-4-yl) (phenyl)methylene)morpholine-4-carbothiohydrazide (KS-10031)
  - Synthesis of bis(2-methylthiazol-4-yl)methanol (6)
  - Synthesis of bis(2-methylthiazol-4-yl)methanone (7)
  - Synthesis of methyl 2-(bis(2-methylthiazol-4-yl)methylene)hydrazine-1-carbodithioate (8)
  - Synthesis of 2-(bis(2-methylthiazol-4-yl)methylene)-*N*-methyl-*N*-(tetrahydro-2*H*-pyran-4-yl)hydrazine-1-carbothioamide (KS-10076)
  - Synthesis of $[Zn(KS10076)_2]$
  - Synthesis of $[Fe(KS10076)_2]PF_6$
  - Cytotoxicity test
  - Density functional theory calculation
  - Bioinformatical analysis of RNA-seq data
  - ROS measurement
  - Transmission electron microscope
  - Measurement of oxidative phosphorylation and glycolysis
  - Organelle staining
  - Immunocytochemistry
  - Cycloheximide assay
  - Ubiquitination and immunoprecipitation
  - Antioxidant rescuing assay
  - 3D spheroid assay
  - Organoid culture and viability test
  - Animal experiments
- QUANTIFICATION AND STATISTICAL ANALYSIS

SUPPLEMENTAL INFORMATION

Supplemental information can be found online at https://doi.org/10.1016/j.celrep.2022.111077.

ACKNOWLEDGMENTS

We are grateful to all of the supporting faculty, staff, and colleagues. We appreciate Dr. Doo-Young Jung (PinotBIO). We thank Hongjeong Yoon and Choongkun Lee for the invaluable support and intellectual contributions. In addition, we thank Dr. Dongwook Kim (IBS, Korea) for helpful discussion and experimental support for single X-ray crystallographic analysis. This research was supported by PinotBIO (IIT21-23).

AUTHOR CONTRIBUTIONS

J.K., A.P., H.L., and S.J.S. conceived the project, analyzed and interpreted the data, and wrote the manuscript. J.K., H.W.K., X.Z., and J.L. contributed to the acquisition and analysis of data. J.H., J.K., M.K., J.Y., and U.C. provided technical support. T.I.K. provided material support of the clinical samples. All authors reviewed the results and approved the final version of the manuscript.

DECLARATION OF INTERESTS

H.L. and S.J.S. report research funding from PinotBIO. A.P., J.K., H.L., and S.J.S. have a patent of KS10076.

Received: May 24, 2021
Revised: March 17, 2022
Accepted: June 20, 2022
Published: July 19, 2022

REFERENCES

Basu, S., Singh, M.K., Singh, T.B., Bhartiya, S.K., Singh, S.P., and Shukla, V.K. (2013). Heavy and trace metals in carcinoma of the gallbladder. World J. Surg. *37*, 2641–2646. https://doi.org/10.1007/s00268-013-2164-9.

B'Chir, W., Maurin, A.C., Carraro, V., Averous, J., Jousse, C., Muranishi, Y., Parry, L., Stepien, G., Fafournoux, P., and Bruhat, A. (2013). The eIF2α/ATF4 pathway is essential for stress-induced autophagy gene expression. Nucleic Acids Res. *41*, 7683–7699.

Bernhardt, P.V., Sharpe, P.C., Islam, M., Lovejoy, D.B., Kalinowski, D.S., and Richardson, D.R. (2009). Iron chelators of the dipyridylketone thiosemicarbazone class: precomplexation and transmetalation effects on anticancer activity. J. Med. Chem. *52*, 407–415. https://doi.org/10.1021/jm801012z.

Bormio Nenes, J.H., Hager, S., Mathuber, M., Pósa, V., Roller, A., Enyedy, É.A., Stefanelli, A., Berger, W., Keppler, B.K., Heffeter, P., and Kowol, C.R. (2020). Cancer cell resistance against the clinically investigated thiosemicarbazone COTI-2 is based on formation of intracellular Copper complex glutathione adducts and ABCC1-mediated efflux. J. Med. Chem. *63*, 13719–13732. https://doi.org/10.1021/acs.jmedchem.0c01277.

Bryant, K.L., Stalnecker, C.A., Zeitouni, D., Klomp, J.E., Peng, S., Tikunov, A.P., Gunda, V., Pierobon, M., Waters, A.M., George, S.D., et al. (2019). Combination of ERK and autophagy inhibition as a treatment approach for pancreatic cancer. Nat. Med. *25*, 628–640. https://doi.org/10.1038/s41591-019-0368-8.

Cheng, Z., Dai, L.L., Song, Y.N., Kang, Y., Si, J.M., Xia, J., and Liu, Y.F. (2014). Regulatory effect of iron regulatory protein-2 on iron metabolism in lung cancer. Genet. Mol. Res. *13*, 5514–5522. https://doi.org/10.4238/2014.july.25.5.

Crisponi, G., Nurchi, V.M., and Lachowicz, J.I. (2019). In 3. Iron Chelation for Iron Overload in Thalassemia, P.L. Carver, ed. (De Gruyter), pp. 49–86.

Gargalovic, P.S., Imura, M., Zhang, B., Gharavi, N.M., Clark, M.J., Pagnon, J., Yang, W.P., He, A., Truong, A., Patel, S., et al. (2006). Identification of inflammatory gene modules based on variations of human endothelial cell responses to oxidized lipids. Proc. Natl. Acad. Sci. USA *103*, 12741–12746. https://doi.org/10.1073/pnas.0605457103.

Griess, B., Tom, E., Domann, F., and Teoh-Fitzgerald, M. (2017). Extracellular superoxide dismutase and its role in cancer. Free Radic. Biol. Med. *112*, 464–479. https://doi.org/10.1016/j.freeradbiomed.2017.08.013.

Harhous, Z., Booz, G.W., Ovize, M., Bidaux, G., and Kurdi, M. (2019). An update on the multifaceted roles of STAT3 in the heart. Front. Cardiovasc. Med. *6*, 150. https://doi.org/10.3389/fcvm.2019.00150.

Ibrahim, O., and O'Sullivan, J. (2020). Iron chelators in cancer therapy. Biometals *33*, 201–215. https://doi.org/10.1007/s10534-020-00243-3.

Jang, H.H. (2018). Regulation of protein degradation by proteasomes in cancer. J. Cancer Prev. *23*, 153–161. https://doi.org/10.15430/jcp.2018.23.4.153.

Jansson, P.J., Sharpe, P.C., Bernhardt, P.V., and Richardson, D.R. (2010). Novel thiosemicarbazones of the ApT and DpT series and their copper complexes: identification of pronounced redox activity and characterization of their antitumor activity. J. Med. Chem. *53*, 5759–5769. https://doi.org/10.1021/jm100561b.

Jia, J., Claude-Taupin, A., Gu, Y., Choi, S.W., Peters, R., Bissa, B., Mudd, M.H., Allers, L., Pallikkuth, S., Lidke, K.A., et al. (2020a). Galectin-3 coordinates a cellular system for lysosomal repair and removal. Dev. Cell *52*, 69–87.e8. https://doi.org/10.1016/j.devcel.2019.10.025.

Jia, J., Claude-Taupin, A., Gu, Y., Choi, S.W., Peters, R., Bissa, B., Mudd, M.H., Allers, L., Pallikkuth, S., Lidke, K.A., et al. (2020b). Galectin-3 coordinates a cellular system for lysosomal repair and removal. Dev. Cell *52*, 69–87.e8. https://doi.org/10.1016/j.devcel.2019.10.025.

Ju, H.-Q., Lin, J.-F., Tian, T., Xie, D., and Xu, R.-H. (2020). NADPH homeostasis in cancer: functions, mechanisms and therapeutic implications. Signal Transduct. Target Ther. *5*, 231. https://doi.org/10.1038/s41392-020-00326-0.

Jung, T., Höhn, A., and Grune, T. (2014). The proteasome and the degradation of oxidized proteins: part III-Redox regulation of the proteasomal system. Redox Biol. *2*, 388–394. https://doi.org/10.1016/j.redox.2013.12.029.

Kalinowski, D.S., Quach, P., and Richardson, D.R. (2009). Thiosemicarbazones: the new wave in cancer treatment. Future Med. Chem. *1*, 1143–1151. https://doi.org/10.4155/fmc.09.80.

Kalinowski, D.S., Yu, Y., Sharpe, P.C., Islam, M., Liao, Y.-T., Lovejoy, D.B., Kumar, N., Bernhardt, P.V., and Richardson, D.R. (2007). Design, synthesis, and characterization of novel iron chelators: structure-activity relationships of the 2-benzoylpyridine thiosemicarbazone series and their 3-nitrobenzoyl analogues as potent antitumor agents. J. Med. Chem. *50*, 3716–3729. https://doi.org/10.1021/jm070445z.

Keberle, H. (1964). The Biochemistry of desferrioxamine and its relation to iron metabolism. Ann. N. Y. Acad. Sci. *119*, 758–768. https://doi.org/10.1111/j.1749-6632.1965.tb54077.x.

Kinsey, C.G., Camolotto, S.A., Boespflug, A.M., Guillen, K.P., Foth, M., Truong, A., Schuman, S.S., Shea, J.E., Seipp, M.T., Yap, J.T., et al. (2019). Protective autophagy elicited by RAF→MEK→ERK inhibition suggests a treatment strategy for RAS-driven cancers. Nat. Med. *25*, 620–627. https://doi.org/10.1038/s41591-019-0367-9.

Kirkman, H.N., and Gaetani, G.F. (1984). Catalase: a tetrameric enzyme with four tightly bound molecules of NADPH. Proc. Natl. Acad. Sci. USA *81*, 4343–4347. https://doi.org/10.1073/pnas.81.14.4343.

Kowol, C.R., Berger, R., Eichinger, R., Roller, A., Jakupec, M.A., Schmidt, P.P., Arion, V.B., and Keppler, B.K. (2007). Gallium(III) and iron(III) complexes of α-N-heterocyclic thiosemicarbazones: synthesis, characterization, cytotoxicity, and interaction with ribonucleotide reductase. J. Med. Chem. *50*, 1254–1265. https://doi.org/10.1021/jm0612618.

Lindemann, A., Patel, A.A., Silver, N.L., Tang, L., Liu, Z., Wang, L., Tanaka, N., Rao, X., Takahashi, H., Maduka, N.K., et al. (2019). COTI-2, A novel thiosemicarbazone derivative, exhibits antitumor activity in HNSCC through p53-dependent and -independent mechanisms. Clin. Cancer Res. *25*, 5650–5662. https://doi.org/10.1158/1078-0432.CCR-19-0096.

Lovejoy, D.B., Jansson, P.J., Brunk, U.T., Wong, J., Ponka, P., and Richardson, D.R. (2011). Antitumor activity of metal-chelating compound Dp44mT is mediated by formation of a redox-active copper complex that accumulates in lysosomes. Cancer Res. *71*, 5871–5880. https://doi.org/10.1158/0008-5472.can-11-1218.

Lovejoy, D.N., Sharp, D.M., Seebacher, N., Obeidy, P., Prichard, T., Stefani, C., Basha, M.T., Basha, M.T., Sharpe, P.C., Jansson, P.J., et al. (2012). Novel second-generation di-2-pyridylketone thiosemicarbazones show synergism with standard chemotherapeutics and demonstrate potent activity against lung cancer xenografts after oral and intravenous administration in vivo. J. Med. Chem. *55*, 7230–7244. https://doi.org/10.1021/jm300768u.

Ma, L., Dong, L., and Chang, P. (2019). CD44v6 engages in colorectal cancer progression. Cell Death Dis. *10*, 30. https://doi.org/10.1038/s41419-018-1265-7.

Martinez-Cruzado, L., Tornin, J., Santos, L., Rodriguez, A., García-Castro, J., Morís, F., and Rodriguez, R. (2016). Aldh1 expression and activity increase during tumor evolution in sarcoma cancer stem cell populations. Sci. Rep. *6*, 27878. https://doi.org/10.1038/srep27878.

Martínez-Reyes, I., and Chandel, N.S. (2020). Mitochondrial TCA cycle metabolites control physiology and disease. Nat. Commun. *11*, 102. https://doi.org/10.1038/s41467-019-13668-3.

Merlot, A.M., Kalinowski, D.S., and Richardson, D.R. (2013). Novel chelators for cancer treatment: where are we now? Antioxid. Redox Signal. *18*, 973–1006. https://doi.org/10.1089/ars.2012.4540.

Moreno-Sánchez, R., Gallardo-Pérez, J.C., Rodríguez-Enríquez, S., Saavedra, E., and Marín-Hernández, Á. (2017). Control of the NADPH supply for oxidative stress handling in cancer cells. Free Radic. Biol. Med. *112*, 149–161. https://doi.org/10.1016/j.freeradbiomed.2017.07.018.

Palde, P.B., and Carroll, K.S. (2015). A universal entropy-driven mechanism for thioredoxin-target recognition. Proc. Natl. Acad. Sci. USA *112*, 7960–7965. https://doi.org/10.1073/pnas.1504376112.

Raimondi, V., Ciccarese, F., and Ciminale, V. (2020). Oncogenic pathways and the electron transport chain: a dangeROS liaison. Br. J. Cancer *122*, 168–181. https://doi.org/10.1038/s41416-019-0651-y.

Raini, G., Sharet, R., Herrero, M., Atzmon, A., Shenoy, A., Geiger, T., and Elroy-Stein, O. (2017). Mutant eIF2B leads to impaired mitochondrial oxidative phosphorylation in vanishing white matter disease. J. Neurochem. *141*, 694–707. https://doi.org/10.1111/jnc.14024.

Richardson, D.R., Sharpe, P.C., Lovejoy, D.B., Senaratne, D., Kalinowski, D.S., Islam, M., and Bernhardt, P.V. (2006). Dipyridyl thiosemicarbazone chelators with potent and selective antitumor activity form iron complexes with redox activity. J. Med. Chem. *49*, 6510–6521. https://doi.org/10.1021/jm0606342.

Salim, K.Y., Maleki Vareki, S., Danter, W.R., San-Marina, S., and Koropatnick, J. (2016). COTI-2, a novel small molecule that is active against multiple human cancer cell lines *in vitro* and *in vivo*. Oncotarget *7*, 41363–41379. https://doi.org/10.18632/oncotarget.9133.

Schöpf, B., Weissensteiner, H., Schäfer, G., Fazzini, F., Charoentong, P., Naschberger, A., Rupp, B., Fendt, L., Bukur, V., Giese, I., et al. (2020). OXPHOS remodeling in high-grade prostate cancer involves mtDNA mutations and increased succinate oxidation. Nat. Commun. *11*, 1487. https://doi.org/10.1038/s41467-020-15237-5.

Shakya, B., and Yadav, P.N. (2020). Thiosemicarbazones as potent anticancer agents and their modes of action. Mini Rev. Med. Chem. *20*, 638–661. https://doi.org/10.2174/1389557519666191029130310.

Sobotta, M.C., Liou, W., Stöcker, S., Talwar, D., Oehler, M., Ruppert, T., Scharf, A.N., and Dick, T.P. (2015). Peroxiredoxin-2 and STAT3 form a redox relay for H_2O_2 signaling. Nat. Chem. Biol. *11*, 64–70. https://doi.org/10.1038/nchembio.1695.

Stacy, A.E., Palanimuthu, D., Bernhardt, P.V., Kalinowski, D.S., Jansson, P.J., and Richardson, D.R. (2016). Zinc(II)-thiosemicarbazone complexes are

localized to the lysosomal compartment where they transmetallate with copper ions to induce cytotoxicity. J. Med. Chem. *59*, 4965–4984. https://doi.org/10.1021/acs.jmedchem.6b00238.

Stefani, C., Jansson, P.J., Gutierrez, E., Bernhardt, P.V., Richardson, D.R., and Kalinowski, D.S. (2013). Alkyl substituted 2'-benzoylpyridine thiosemicarbazone chelators with potent and selective anti-neoplastic activity: novel ligands that limit methemoglobin formation. J. Med. Chem. *56*, 357–370. https://doi.org/10.1021/jm301691s.

Torti, S.V., and Torti, F.M. (2013). Iron and cancer: more ore to be mined. Nat. Rev. Cancer *13*, 342–355. https://doi.org/10.1038/nrc3495.

Torti, S.V., Manz, D.H., Paul, B.T., Blanchette-Farra, N., and Torti, F.M. (2018). Iron and cancer. Annu. Rev. Nutr. *38*, 97–125. https://doi.org/10.1146/annurev-nutr-082117-051732.

Turrens, J.F. (2003). Mitochondrial formation of reactive oxygen species. J. Physiol. *552*, 335–344. https://doi.org/10.1113/jphysiol.2003.049478.

Valcarcel-Jimenez, L., Gaude, E., Torrano, V., Frezza, C., and Carracedo, A. (2017). Mitochondrial metabolism: yin and yang for tumor progression. Trends Endocrinol. Metabol. *28*, 748–757. https://doi.org/10.1016/j.tem.2017.06.004.

Wang, H., Shi, H., Rajan, M., Canarie, E.R., Hong, S., Simoneschi, D., Pagano, M., Bush, M.F., Stoll, S., Leibold, E.A., and Zheng, N. (2020). FBXL5 regulates IRP2 stability in iron homeostasis via an oxygen-responsive [2Fe2S] cluster. Mol. Cell *78*, 31–41.e5. https://doi.org/10.1016/j.molcel.2020.02.011.

Xiao, C., Fu, X., Wang, Y., Liu, H., Jiang, Y., Zhao, Z., and You, F. (2020). Transferrin receptor regulates malignancies and the stemness of hepatocellular carcinoma-derived cancer stem-like cells by affecting iron accumulation. PLoS One *15*, e0243812. https://doi.org/10.1371/journal.pone.0243812.

Xu, W., Barrientos, T., and Andrews, N.C. (2013). Iron and copper in mitochondrial diseases. Cell Metabol. *17*, 319–328. https://doi.org/10.1016/j.cmet.2013.02.004.

Yamasaki, T., Terai, S., and Sakaida, I. (2011). Deferoxamine for advanced hepatocellular carcinoma. N. Engl. J. Med. *365*, 576–578. https://doi.org/10.1056/nejmc1105726.

Yu, X., Vazquez, A., Levine, A.J., and Carpizo, D.R. (2012). Allele-specific p53 mutant reactivation. Cancer Cell *21*, 614–625. https://doi.org/10.1016/j.ccr.2012.03.042.

Zhao, R.-Z., Jiang, S., Zhang, L., and Yu, Z.-B. (2019). Mitochondrial electron transport chain, ROS generation and uncoupling (Review). Int. J. Mol. Med. *44*, 3–15. https://doi.org/10.3892/ijmm.2019.4188.

Zong, W.-X., Rabinowitz, J.D., and White, E. (2016). Mitochondria and cancer. Mol. Cell *61*, 667–676. https://doi.org/10.1016/j.molcel.2016.02.011.

STAR★METHODS

KEY RESOURCES TABLE

REAGENT or RESOURCE	SOURCE	IDENTIFIER
Antibodies		
ALDH1A1 (H-4)	Santa Cruz Biotechnology	Cat#sc-374076, RID:AB_10916407
Alpha tubulin (TU-02)	Santa Cruz Biotechnology	Cat#sc-8035, RRID:AB_628408
Anti-c-Abl, phospho (Tyr245)	Cell Signaling Technology	Cat#sc-2861, RRID:AB_331029
ATF4	Cell Signaling Technology	Cat#11815, RRID:AB_2616025
Bcl-2 (C-2)	Santa Cruz Biotechnology	Cat#sc-7382, RRID:AB_626736
CD133 (D4W4N)	Cell Signaling Technology	Cat#86781, RRID:AB_2800092
CD133 (Prominin-1) (TMP4)	Thermo Fisher Scientific	Cat#12-1338-42, RID:AB_1582257
CD44 (156-3C11)	Cell Signaling Technology	Cat#3570, RRID:AB_2076465
CD44 (IM7), APC	Invitrogen	Cat#17-0441-82, RRID:AB_469390
CD44v6 [VFF-18]	Abcam	Cat#ab78960, RRID:1603730
Cdc2 p34 (B-6)	Santa Cruz Biotechnology	Cat#sc-8395, RRID:AB_627225
Cdc25B	Cell Signaling Technology	Cat#9525, RRID:AB_10694926
Cleaved Caspase-3 (Asp175) (5A1E)	Cell Signaling Technology	Cat#9664, RRID:AB_2070042
c-Myc (9E10)	Santa Cruz Biotechnology	Cat#sc-40, RRID:AB_2857941
Cyclin B1 (GNS1)	Santa Cruz Biotechnology	Cat#sc-245, RRID:AB_627338
Cyclin D1 (92G2)	Cell Signaling Technology	Cat#2978, RRID:AB_2259616
E-Cadherin (24E10)	Cell Signaling Technology	Cat#3195, RRID:AB_2291471
eIF2 alpha	Cell Signaling Technology	Cat#9722, RRID:AB_2230924
FOXM1 (A-11)	Santa Cruz Biotechnology	Cat#sc-271746, RID:AB_10708585
FTH1	Cell Signaling Technology	Cat#3998, RRID:AB_1903974
GAPDH (6C5)	Santa Cruz Biotechnology	Cat#sc-32233, RRID:AB_627679
Glutathione Peroxidase 4 [EPNCIR144]	Abcam	Cat#ab125066, RRID:AB_10973901
Goat anti-Mouse IgG (H+L), Alexa Fluor 488	Invitrogen	Cat#A-11001, RRID:AB_2534069
Goat anti-Mouse IgG (H + L), Texas Red	Invitrogen	Cat#T6390, RRID:AB_1500646
Goat anti-Rabbit IgG (H + L), Alexa Fluor 488	Invitrogen	Cat#A11008, RRID:AB_143165
Goat anti-Rabbit IgG (H + L), Texas Red	Invitrogen	Cat#T2767, RRID:AB_221655
GP130	Cell Signaling Technology	Cat#3732, RRID:AB_2125953
HA-Tag (F-7)	Santa Cruz Biotechnology	Cat#sc-7392, RRID:AB_627809
HDAC2 (D6S5P)	Cell Signaling Technology	Cat#57156, RRID:AB_2756828
HIF-1alpha (C-Term)	Cayman Chemical	Cat#10006421, RRID:AB_409037
HIF-2alpha (D9E3)	Cell Signaling Technology	Cat#7096, RRID:AB_10898028
HO-1 (D60G11)	Cell Signaling Technology	Cat#5853, RRID:AB_10835857
IRP-2 (7H6)	Santa Cruz Biotechnology	Cat#sc-33682, RRID:AB_2126703
Jak1	Cell Signaling Technology	Cat#3332, RRID:AB_2128499
Keap1 (G-2)	Santa Cruz Biotechnology	Cat#sc-365626, RID:AB_10844829
Ki67 [SP6]	Abcam	Cat#ab16667, RRID:AB_302459
Lamin B1 (A-11)	Santa Cruz Biotechnology	Cat#sc-377000, RRID:AB_2861346
LC3B	Cell Signaling Technology	Cat#2775, RRID:AB_915950
Met	Cell Signaling Technology	Cat#3127, RRID:AB_331361
Anti-SOD-2, Clone E-10	Santa Cruz Biotechnology	Cat#sc-137254, RRID:AB_2191808
mTOR (7C10)	Cell Signaling Technology	Cat#2983, RRID:AB_2105622
N-Cadherin (D4R1H)	Cell Signaling Technology	Cat#13116, RRID:AB_2687616

(*Continued on next page*)

Continued

REAGENT or RESOURCE	SOURCE	IDENTIFIER
NDRG1 (D6C2)	Cell Signaling Technology	Cat#9408, RRID:AB_11140640
NFE2L2	Abcam	Cat#ab62352, RRID:AB_944418
NQO1 (A180)	Santa Cruz Biotechnology	Cat#sc-32793, RRID:AB_628036
Phospho-Cdc2 (Tyr15) (10A11)	Cell Signaling Technology	Cat#4539, RRID:AB_560953
Phospho-eIF2alpha (Ser51)	Cell Signaling Technology	Cat#9721, RRID:AB_330951
Phospho-Jak1 (Tyr1022/1023)	Cell Signaling Technology	Cat#3331, RRID:AB_2265057
Phospho-Jak2 (Tyr1007/1008) (C80C3)	Cell Signaling Technology	Cat#sc-3776, RRID:AB_2617123
Phospho-LATS1 (Ser909)	Cell Signaling Technology	Cat#9157, RRID:AB_2133515
Phospho-mTOR (Ser2448) (D9C2)	Cell Signaling Technology	Cat#5536, RRID:AB_10691552
Phospho-mTOR (Ser2448)	Cell Signaling Technology	Cat#2971, RRID:AB_330970
Phospho-Src (Tyr416) (D49G4)	Cell Signaling Technology	Cat#6943, RRID:AB_10013641
Phospho-Stat3 (Tyr705) (D3A7)	Cell Signaling Technology	Cat#9145, RRID:AB_2491009
Phospho-YAP (Ser127)	Cell Signaling Technology	Cat#4911, RRID:AB_2218913
Anti-Met, phospho (Tyr1234/Tyr1235), Clone D26	Cell Signaling Technology	Cat#3077, RRID:AB_2143884
SOD2 (D9V9C)	Cell Signaling Technology	Cat#13194, RRID:AB_2750869
Src (36D10)	Cell Signaling Technology	Cat#2109, RRID:AB_2106059
Stat3 (D1B2J)	Cell Signaling Technology	Cat#30835, RRID:AB_2798995
SQSTM1 (P62) (D3)	Santa Cruz Biotechnology	Cat#sc-28359, RRID:AB_628279
Transferrin Receptor 1 (10F11)	Thermo Fisher Scientific	Cat#MA5-11441, RID:AB_10966364
Twist (Twist2C1a)	Santa Cruz Biotechnology	Cat#sc-81417, RRID:AB_1130910
Ubiquitin (P4D1)	Cell Signaling Technology	Cat#sc-8017, RRID:AB_2762364
Vimentin (RV202)	Santa Cruz Biotechnology	Cat#sc-32233, RRID:AB_628436
xCT	Abcam	Cat#ab37185, RRID:AB_778944
YAP (D8H1X)	Cell Signaling Technology	Cat#14074, RRID:AB_2650491
β-Actin (C4)	Santa Cruz Biotechnology	Cat#sc-47778, RRID:AB_2714189
Chemicals, peptides, and recombinant proteins		
KS10031	This study	NA
KS10076	This study	NA
Dp44mT	Sigma Aldrich	Cat#SML0186
DpC	Sigma Aldrich	Cat#SML0483
Deferoxamine mesylate salt	Sigma Aldrich	Cat#D9533
JSI-124	ChemNorm	Cat#TBW00963
Triapine	ChemNorm	Cat#TBW02846
Stattic	BLD Pharmtech	Cat#BD109824
Z-VAD-FMK	BLD Pharmtech	Cat#BP305664
Ferrostatin-1	ChemNorm	Cat#TBW02865
Choloquine	Medchem Express	HY-175895A
Necrostatin-1	ChemNorm	Cat#TBW02864
Necrosulfonamide	ChemNorm	Cat#TBW02863
MG-132	Sigma Aldrich	Cat#M7449
Matrigel	Corning	Cat#354230
Human TGF beta 1	Peprotech	Cat#100-21-02
Human EGF	Peprotech	Cat#100-47-500
Y27632	Peprotech	Cat#1293823
N2 supplement (100X)	Thermo Fisher Scientific	Cat#17502048
B27 supplement (50X)	Thermo Fisher Scientific	Cat#17504044

(*Continued on next page*)

Continued

REAGENT or RESOURCE	SOURCE	IDENTIFIER
L-Glutamine	Sigma Aldrich	Cat#G7513
SB202190	Sigma Aldrich	Cat#S7067
DMEM F/12	Lonza	Cat#12-719F
TrypLE EXPRESS	Gibco	Cat#12605028
A83-01	Sigma Aldrich	Cat#SML0788
Ammonium persulfate	Sigma Aldrich	Cat#A3678
TEMED	Sigma Aldrich	Cat#T7024
Triton X-100	Sigma Aldrich	Cat#93443
Acrylamide:bis 30%, 29:1	Genedepot	Cat#A0418-050
Protease inhibitor	Genedepot	Cat#A3100-005
Protein marker	Genedepot	Cat#A8500-040
Protein extraction solution (RIPA)	ELPIS	Cat#EBA-1149
Lipofectamine 3000	Invitrogen	Cat#L3000-015
Fructose	Sigma Aldrich	Cat#F0127
MitoSOX™ Red Mitochondiral Superoxide Indicator	Invitrogen	Cat#M36008
CM-H2DCFDA	Invitrogen	Cat#C6827
MitoTracker™ Red	Invitrogen	Cat#M7512
LysoTracker™ Green DND-26	Invitrogen	Cat#L7526
Dynabeads™ Protein G	Invitrogen	Cat#10003D
DynaMag™-2 Magnet	Invitrogen	Cat#12321D
N-Ethylmaleimide	Thermo Fisher Scientific	Cat#23030
Paraformaldehyde	Tech&Innovation	Cat#BPP-9004
N-acetyl-L-cysteine	Sigma Aldrich	Cat#A7250
Mitoquinol	Cayman Chemical	Cat#89950
Cycloheximide	Sigma Aldrich	Cat#01810
SYBR™ Green PCR Master Mix	Applied Biosystems	Cat#4309155
Heochst33342	Invitrogen	Cat#H1399
Calcein AM	Invitrogen	Cat#C3099
EthD-1	Invitrogen	Cat#E1169
Poly-HEMA	Sigma Aldrich	Cat#P3932
Critical commercial assays		
Cell Counting Kit-8 assay kit	Dojindo	Cat#CK04
High-Capacity cDNA Reverse Transcription kit	Applied Biosystems	Cat#4368814
Superoxide Dismutase Activity assay kit	Abcam	Cat#ab65354
Deposited data		
Raw RNA-seq data of KS10076-treated cell lines	This study	https://data.mendeley.com/datasets/5vhjg6gtvr/draft?a=432e0920-a41a-4b60-8a39-de6bf8724d4f
CCLE gene expression data	https://depmap.org/portal/download	Expression Public 20Q3
Experimental models: Cell lines		
PFEIFFER	ATCC	Cat# CRL-2632, RRID:CVCL_3326
KARPAS299	ECACC	Cat# 06072604, RRID:CVCL_1324
HCT116	ATCC	Cat# CCL-247, RRID:CVCL_0291
COLO201	Korean Cell Line Bank	Cat# 10224, RRID:CVCL_1987
SNUC1	Korean Cell Line Bank	Cat# 0000C1, RRID:CVCL_1708
COLO205	ATCC	Cat# CCL-222, RRID:CVCL_0218

(*Continued on next page*)

Continued

REAGENT or RESOURCE	SOURCE	IDENTIFIER
LS1034	ATCC	Cat# CRL-2158, RRID:CVCL_1382
CAKI1	ATCC	Cat# HTB-46, RRID:CVCL_0234
CAKI2	ATCC	Cat# HTB-47, RRID:CVCL_0235
EFM192A	DSMZ	Cat# ACC-258, RRID:CVCL_1812
SW480	ATCC	Cat# CCL-228, RRID:CVCL_0546
Experimental models: Organisms/strains		
Mouse: BALB/c Nude Mice	ORIENT BIO	NA
Human: Yonsei Cancer Organoid (YCO)	Yonsei University	NA
Recombinant DNA		
pCNS-D2 STAT3 (F)	Korea Human Gene Bank	BKU002144
HA-Ubiquitin	Addgene	Cat#18712
pcDNA3-mRFP	Addgene	Cat#13032
Myc-Galectin-3	Origene	Cat#RC208785
Software and algorithms		
GraphPad Prism 5.0	GraphPad	NA
R	www.r-project.org	NA
GSEA	http://software.broadinstitute.org	NA
Harmony 4.9	PerkinElmer	NA
Other		
Operetta CLS	PerkinElmer	NA

RESOURCE AVAILABILITY

Lead contact

Further information and requests for resources and reagents should be directed to and will be fulfilled by the lead contact, Sang Joon Shin (ssj338@yuhs.ac).

Materials availability

All reagents generated in this study are available from the lead contact with a completed Materials Transfer Agreement.

Data and code availability

- RNA-seq data have been deposited on Mendeley at [https://data.mendeley.com/datasets/5vhjg6gtvr/draft?a=432e0920-a41a-4b60-8a39-de6bf8724d4f] and are publicly available as of the date of publication. The DOI is listed in the key resources table.
- This paper does not report original code.
- Any additional information required to reanalyze the data reported in this paper is available from the lead contact upon request.

EXPERIMENTAL MODEL AND SUBJECT DETAILS

Cell lines

HCT116 and SW480 were grown in Dulbecco's modified Eagle medium (DMEM) supplemented with 10% fetal bovine serum (FBS), 100 U/mL penicillin, and 100 μg/mL streptomycin. CAKI2 were grown in RPMI1640 supplemented with 10% FBS, 100 U/mL penicillin, 100 μg/mL streptomycin, and 1× glutamax. PFEIFFER, KARPAS299, COLO201, COLO205, SNUC1, LS1034, CAKI1, and EFM192A were cultured in RPMI1640 containing 10% FBS, 100 U/mL penicillin, and 100 μg/mL streptomycin.

Mice

Male mice (5 weeks old) were used for experiment. All mice were housed in accordance with policies approved by the Animal ethics committee of Yonsei College of Medicine.

METHOD DETAILS

Synthesis of KS10031 and KS10076[a]

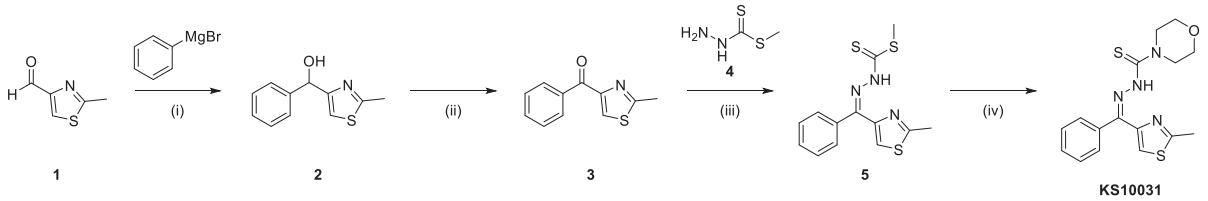

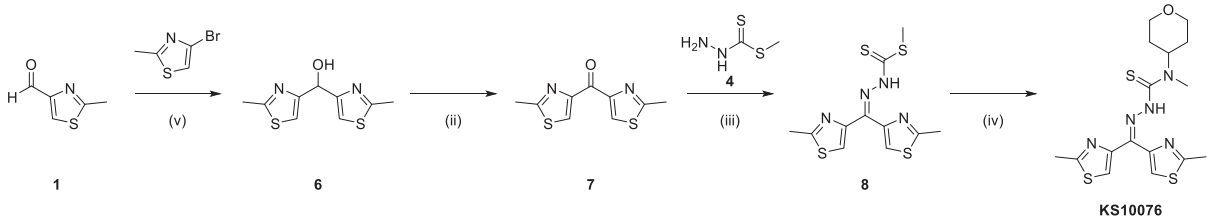

[a]Reagents and conditions: (i) THF, −20°C to rt, 20 h, 99%; (ii) MnO_2, DCM, rt, 12 h, 76%; (iii) AcOH, MeOH, 50°C, 24 h, 93%; (iv) EtOH, reflux, 24 h, 68%; (v) *n*-BuLi, Ether/THF, −78°C to rt, 3 h, 40%.

Synthesis of (2-methylthiazol-4-yl) (phenyl)methanol (2)

To a solution of 2-methylthizole-4-carbaldehyde (3.8 g, 30.0 mmol, 1.0 equiv) in THF (50 mL) was added dropwise phenylmagnesium bromide (1.0 M in THF, 33 mL, 33.0 mmol, 1.1 equiv) at −20°C under argon. The reaction mixture was stirred at room temperature for 20 h. The reaction mixture was carefully quenched by addition of saturated aqueous NH_4Cl solution at 0°C. After stirring for 5 min at 0°C, the reaction mixture was poured into H_2O and extracted with EtOAc. The organic layer was washed with brine, dried over $MgSO_4$, filtered, and evaporated under reduced pressure to obtain the desired product as a brown oil (6.15 g, 99%).

Synthesis of (2-methylthiazol-4-yl) (phenyl)methanone (3)

To a solution of **2** (6.15 g, 30.0 mmol, 1.0 equiv) in DCM (300 mL) was added MnO_2 (26 g, 300.0 mmol, 10.0 equiv) in 10 portions at 0°C. The reaction mixture was stirred at room temperature for 12 h. The reaction mixture was filtered through a pad of Celite, evaporated under reduced pressure, and the residue was purified by flash column chromatography to obtain the desired product as a yellow oil (4.62 g, 76%).

Synthesis of methyl hydrazinecarbodithioate (4)

To a solution of KOH (11.2 g, 200.0 mmol, 1.0 equiv) in *i*-PrOH/H_2O (15/15 mL) was added hydrazine monohydrate (10.0 mL, 200.0 mmol, 1.0 equiv) at 0°C. Carbon disulfide (12.1 mL, 200.0 mmol, 1.0 equiv) was added dropwise over 1 h and stirred for 1 h at <10°C, then iodomethane (12.7 mL, 200.0 mmol, 1.0 equiv) was added over 1 h and stirred for 2 h at <10°C. The solids were filtered and washed with H_2O The crude solid was dissolved in THF, dried over $MgSO_4$, filtered, and evaporated under reduced pressure. The crude product was recrystallized from DCM to obtain the desired product as a white solid (13.3 g, 54%).

Synthesis of methyl 2-((2-methylthiazol-4-yl) (phenyl)methylene)hydrazine-1-carbodithioate (5)

To a mixture of **3** (4.67 g, 23.0 mmol, 1.0 equiv) and **4** (8.43 g, 69.0 mmol, 3.0 equiv) in MeOH (200 mL) was added AcOH (5 drops). The reaction mixture was stirred at 50°C for 24 h. The reaction mixture was filtered with MeOH to obtain the desired product as a yellow solid (6.57 g, 93%).

Synthesis of *N*'-((2-methylthiazol-4-yl) (phenyl)methylene)morpholine-4-carbothiohydrazide (KS-10031)

The mixture of **5** (6.15 g, 20.0 mmol, 1.0 equiv) and morpholine (8.7 mL, 100.0 mmol, 5.0 equiv) in EtOH (200 mL) was refluxed for 24 h. The reaction mixture was evaporated under reduced pressure and purified by flash column chromatography. The crude was solidified with MeOH to obtain the desired product as a yellow solid (4.76 g, 68%).

^{1}H NMR (300 MHz, DMSO-d_6) δ 13.30 (s, 1H), 7.67 (s, 1H), 7.61–7.57 (m, 2H), 7.50–7.46 (m, 3H), 4.00–3.96 (m, 4H), 3.72–3.68 (m, 4H), 2.81 (s, 3H).

Synthesis of bis(2-methylthiazol-4-yl)methanol (6)

To a solution of 4-bromo2-methylthizole (3.1 mL, 30.0 mmol, 1.0 equiv) in dried Et_2O (50 mL) was added dropwise *n*-butyllithium (2.0 M in cyclohexane, 18 mL, 36.0 mmol, 1.2 equiv) at −78°C under argon. The reaction mixture was stirred at −78°C for 5 min. To the reaction mixture was added dropwise a solution of 2-methylthizole-4-carbaldehyde (3.81 g, 30.0 mmol, 1.0 equiv) in THF (25 mL) at −78°C. The reaction mixture was stirred at room temperature for 3 h and was carefully quenched by the addition of saturated aqueous NH_4Cl solution at 0°C. After stirring for 5 min at 0°C, the mixture was poured into H_2O and extracted with EtOAc. The organic layer was washed with brine, dried over $MgSO_4$, filtered, and evaporated under reduced pressure. The residue was purified by flash column chromatography to obtain the desired product as a beige solid (2.74 g, 40%).

Synthesis of bis(2-methylthiazol-4-yl)methanone (7)

The compound was synthesized from **6** (2.74 g, 12.1 mmol) to yield as a yellow oil (2.05 g, 76%).

Synthesis of methyl 2-(bis(2-methylthiazol-4-yl)methylene)hydrazine-1-carbodithioate (8)

The compound was synthesized from **7** (2.05 g, 9.1 mmol) to yield as a yellow solid (2.57 g, 86%).

Synthesis of 2-(bis(2-methylthiazol-4-yl)methylene)-*N*-methyl-*N*-(tetrahydro-2*H*-pyran-4-yl)hydrazine-1-carbothioamide (KS-10076)

The compound was synthesized from **8** (2.57 g, 7.8 mmol) to yield as a yellow solid (1.88 g, 61%).

^{1}H NMR (300 MHz, DMSO-d_6) δ 13.82 (s, 1H), 8.35 (s, 1H), 7.78 (s, 1H), 3.98–3.92 (m, 2H), 3.43–3.35 (m, 2H), 3.18 (s, 3H), 2.82–2.78 (m, 4H), 2.74 (s, 3H), 1.86–1.74 (m, 2H), 1.66–1.62 (m, 2H); ^{13}C NMR (100 MHz, DMSO-d_6) δ 180.0, 166.9, 165.6, 152.3, 147.0, 145.3, 145.3, 135.8, 126.5, 119.8, 67.0, 57.3, 33.2, 29.8, 19.5, 19.2; HRMS (EI) calcd. For $C_{16}H_{21}N_5OS_3$ $[M]^+$ 395.0908, found 395.0903 (Figure S8, NMR spectrum).

Synthesis of [Zn(KS10076)$_2$]

To a 20 mL scintillation vial containing $Zn(SO_4)_2 \cdot 7H_2O$ (58 mg, 0.2 mmol), KS10076 (158 mg, 0.4 mmol) were added EtOH (5 mL), trimethylamine (140 μL, 1.0 mmol). The resulting vial was sealed, and the mixture was stirred for 1 h at 80°C. The resulting precipitate was filtered off and washed with cold EtOH to afford [Zn(KS10076)$_2$] as a yellow solid (38 mg, 22%). Single crystal suitable for X-ray diffraction was obtained from DCM/MeCN (CCDC deposit number: 2150436).

^{1}H NMR (300 MHz, $CDCl_3$) δ 8.88 (s, 2H), 8.29 (s, 2H), 5.32–5.24 (m, 2H), 4.03–3.99 (m, 4H), 3.50–3.41 (m, 4H), 3.18 (s, 6H), 2.81 (s, 6H), 2.30 (s, 6H), 1.91–1.67 (m, 8H).

Synthesis of [Fe(KS10076)$_2$]PF_6

[Fe(KS10076)$_2$]PF_6 was synthesized using previously reported method (Kowol et al., 2007). To a 20 mL scintillation vial containing $Fe(NO_3)_3 \cdot 9H_2O$ (67 mg, 0.17 mmol), KS10076 (118 mg, 0.31 mmol) were added EtOH (5 mL). The resulting vial was sealed, and the mixture was stirred for 5 h at 25°C. To the resulting mixture was added NH_4PF_6 (100 mg, 0.61 mmol) and stirred for 45 min at 25°C. The dark green precipitate was filtered off and washed with cold EtOH to afford [Fe(KS10076)$_2$]PF_6. The [Fe(KS10076)$_2$]PF_6 was further purified by recrystallization from MeCN.

Cytotoxicity test

11 pan-cancer cell lines (PFEIFFER, KARPAS299, HCT116, SW480, COLO205, LS1034, SNUC1, COLO201, EFM192A, CAKI1, and CAKI2) seeded on 96-well plates were incubated with metal chelators at 9 sequential concentrations (0, 0.001, 0.003, 0.01, 0.03, 0.1, 0.3, 1, 3 μM). After 48 h, 10 μL of CCK-8 is added to each well and cells are incubated for 2 h at 37°C before measuring the colorimetry at 450 nm, the OD value of which reflect cell proliferation status. The compounds library (totaling 82) was synthesized and obtained from the Korea Research Institute of Chemical Technology (KRICT).

Density functional theory calculation

The density functional theory (DFT) calculations were performed as implemented in Q-Chem software package. We empolyed B3LYP functional. 6-31G(d,p) basis set was adopted for main group elements and LANL2DZ basis set and effective core potential were used for transition metal elements. Reported energy values were computed at the gas phase and electronic energies were corrected by an implicit solvation model, conductor-like polarizable continuum model (C-PCM).

Bioinformatical analysis of RNA-seq data

The total RNA from KS10076-treated cells (three biological replicates, n = 3) were used for RNA-seq. Transcriptomes of 36 samples were analyzed by RNA-seq (Macrogen Inc.) using Illumina Hiseq 2500 system.

To analyze the genetic profile features affecting metal chelator drug-sensitivity, gene set enrichment analysis is performed using R package GSEA. For RNA-seq data analysis, GSEA v4.0.3 is used with h.all.v7.0.symbols.gmt and c2.cp.kegg.v6.1.symbols.gmt matrix of gene set size from 15 to 500 genes.

ROS measurement

Live HCT116 cells in 96-well plates were stained using ROS detection dyes (CM-DCFDA (cellular) and MITOSOX (Mitochondrial ROS)) at 5 μM for 1 h at 37°C in growth media without phenol. Cells were washed three times with PBS and then imaged using Operetta CLS. Fluorescence was quantitatively analyzed by randomly selecting six fields with three biological replicates using Harmony.

Transmission electron microscope

HCT116 cell was treated with KS10076 (3 μM) for 24 h. The cell was fixed with 2% PFA including 2% glutaraldehyde. The cell was then monitored using transmission electron microscope.

Measurement of oxidative phosphorylation and glycolysis

Cells were treated with KS10076 (0.3, 3 μM) for 24 h and medium was replaced with the XF assay medium including glucose (4.5 g/L), glutamine (4 mM), and sodium pyruvate (1 mM). Oxygen consumption rate (OCR) was analyzed using a Seahorse Biosciences XF^{e} Analyzer.

For measurement of glycolysis, extracellular acidification rate (ECAR) level was determined by adding glucose (80 mM), oligomycin (5 mM), and 2-deoxyglucose (2-DG) (100 mM).

Organelle staining

HCT116 cell and galectin-3-mRFP transgenic HCT116 cell line were treated with KS10076. Then, cells were stained with MitoTracker (mitochondria; final 50 nM), LysoTracker (lysosome; final 50 nM), and Hoechst 33,342 (nucleus; final 300 nM) in PBS for 30 min at RT. The cells with 3 biological replicates (random 6 fields at 40× magnification for each) were imaged using Operetta CLS and Harmony.

Immunocytochemistry

KS10076-pretreated HCT116 cells were fixed using 4% PFA and permeabilized using 0.3% Triton X-100 in PBS for 30 min, respectively, at RT. The samples were blocked using 5% BSA in PBS buffer for 1 h at RT and then incubated with primary antibodies (1:500) in 3% BSA containing 0.1% PBST for 2 h at RT. After washing three times with 0.1% PBST, the secondary antibodies (1:200) and DAPI (500nM) in 3% BSA containing 0.1% PBST were applied and incubated for 1 h at RT. Samples (with 3 biological replicates) were imaged using Operetta CLS at 6 randomly-selected fields.

Cycloheximide assay

HCT116 cells on 100 mm dishes were treated with KS10076 in the presence of cycloheximide 10uM to halt protein translation for protein stability evaluation. After 2, 4, 6, and 12 h of treatment, samples were harvested, lysed using a RIPA buffer with protease and phosphatase inhibitors, and were immunoblotted with antibodies against STAT3 and β-actin (internal control). Then, protein stability changed under the effect of metal chelation was measured via a time-course analysis after halting protein translation.

Ubiquitination and immunoprecipitation

HCT116 cells on 100 mm dishes were transfected with HA-ubiquitin plasmid using PEI (DNA:PEI = 1:2) and incubated for 24 h. Then, cells were treated with KS10076 for 2 h with or without MG132 and harvested. The cells were lysed using a RIPA buffer with protease and phosphatase inhibitors, and were subjected to immunoprecipitation using antibody against STAT3 by incubating with dynamagnetic beads (#10003D, Invitrogen) for 2 h at room temperature. Then, the lysates were subjected to SDS-PAGE and immunoblotting using antibodies against ubiquitin and HA.

Antioxidant rescuing assay

N-acetyl cysteine (NAC; antioxidant against cellular ROS) and MitoQ (antioxidant against mitochondrial ROS) were used to determine the cytotoxic effect on excess ROS induced by KS10076. NAC was added to fresh culture media (DMEM) at 5 mM and the pH was readjusted by adding filtered NaOH. NAC was cotreated with KS10076 for 48 h, and 30-nM MitoQ was added 6 h after KS10076 treatment for 24 h. Then, CCK-8 proliferation assay, CHX assays, and immunoblotting of cancer stem cell markers were conducted to examine if the metal chelation effect is rescued by antioxidants.

3D spheroid assay

To produce spheres with uniform size, 5000 cells/well were seeded in 96 well plates coated with poly-HEMA for low attachment. The plates were centrifuged for 10 min at 1000 rpm immediately. To test the toxicity on true 3D spheroids, cells were grown until each spheroid was clearly visible as a single object of size greater than 400um in diameter. Well-formed spheres were treated with KS10076 (3uM) three times, every three days. The spheroids were monitored in a bright field for a time-course analysis. To examine the population of live and dead cells, the spheroids were stained with calcein AM, ethidium homodimer-1, and Hoechst 33342 for 2 h at 37°C. All measurements and analysis were done using Operetta CLS and Harmony v4.9.

Organoid culture and viability test

Patient-derived organoid culture experiments were approved by the Institutional Review Board of Yonsei University College of Medicine, Severance Hospital (IRB 4-2012-0859). Organoids were grown in DMEM/F12 with 1% penicillin/streptomycin; 1 × Glutamax; 1 × N2 and 1 × B27 supplement; 2 mM L-glutamine; 1 mM N-Acetyl-L-cysteine, 10 mM Nicotinamide; 10 nM Gastrin I; 10 μM SB202190; 500 nM A83-01; 50 ng/mL EGF; and 100 ng/mL Noggin. Organoid cells were cultured in 24 wells in 3D matrix of matrigel (40 μL per well) submerged in 800 ul of organoid growth media. Media was changed every 4 days and organoids were subcultured when the confluency exceeded 70%. For the cytotoxicity test, organoids were seeded on 96-well plates without rocking in 10 ul of matrigel to form a matrix dome. After plating, organoids were incubated in organoid media for 24 h. Then, media were changed into fresh media containing KS10076 (0, 0.0003, 0.001, 0.003, 0.01, 0.03, 1 or 3 μM) and incubated for 5 days. On day 5, a Cell-Titer Glo solution was added to each well, incubated at 37°C for 3 h and measured using a microplate reader.

Animal experiments

Animal studies were approved by the Animal ethics committee of Yonsei College of Medicine. Male nude mice (5 weeks old) were purchased from Orient Bio Inc. (Republic of Korea) and housed in pressurized, ventilated cages with standard rodent chow and water and 12:12 light–dark (LD) cycle. Xenografts were implanted by subcutaneous injection into the flanks of mice using 0.1 mL HCT116 or SW480 cell suspensions (1×10^7 cells/mL) in Matrigel/PBS (1:1) mixture. Mice with tumor volume of 150–250 mm^3 with no general health issues were selected and distributed into vehicle controls and experimental groups. Treatment solutions were prepared in a mixture of dimethyl sulfoxide (#D8418, Sigma-Aldrich, USA), 0.9% saline, and polyethylene glycol 400 (#25322-68-3, Merck, USA) (5:40:55). During the treatment period, tumor volumes were monitored daily and measured bidaily according to the formula: TV (mm^3) = L (mm) × W2 (mm^2) × 1/2. Upon the termination of the experiment, tumors were harvested and subjected to Western blotting.

QUANTIFICATION AND STATISTICAL ANALYSIS

All statistical analyses were performed in GraphPad Prism version 5.0. Results are reported as mean ± SEM of at least three independent experiments. Comparisons were analyzed using an unpaired Student's t-test or one-way analysis of variance (ANOVA) (*$p < 0.05$, **$p < 0.01$, and ***$p < 0.005$), as indicated in the individual figures.

Cell Reports, Volume *40*

Supplemental information

KS10076, a chelator for redox-active metal ions, induces ROS-mediated STAT3 degradation in autophagic cell death and eliminates ALDH1$^+$ stem cells

Jaehee Kim, Areum Park, Jieon Hwang, Xianghua Zhao, Jaesung Kwak, Hyun Woo Kim, Minhee Ku, Jaemoon Yang, Tae Il Kim, Kyu-Sung Jeong, Uyeong Choi, Hyuk Lee, and Sang Joon Shin

A

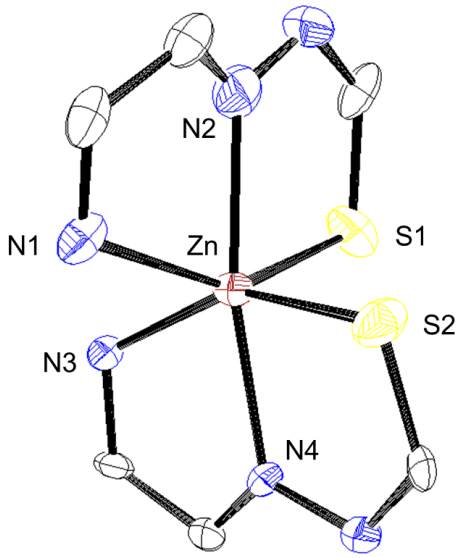

Ligand 1	Zn-N1	Zn-N2	Zn-S1
Distance (Å)	2.213(8)	2.233(8)	2.422(3)
Ligand 2	Zn-N3	Zn-N4	Zn-S2
Distance (Å)	2.153(5)	2.201(7)	2.393(2)

B

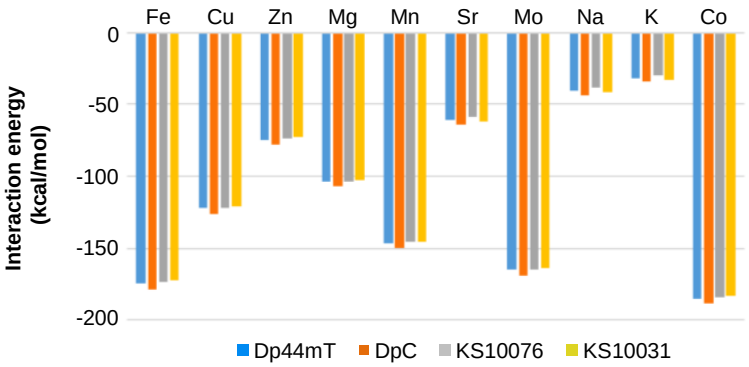

Figure S1. The structural metrics of KS10076 with metal binding affinity, related to Figure 1.

(A) The structural metrics of coordination sphere of [Zn(**KS10076**)$_2$]. (B) Metal binding affinity of Dp44mT, DpC, KS10031, and KS10076 was calculated using density functional theory (DFT).

A

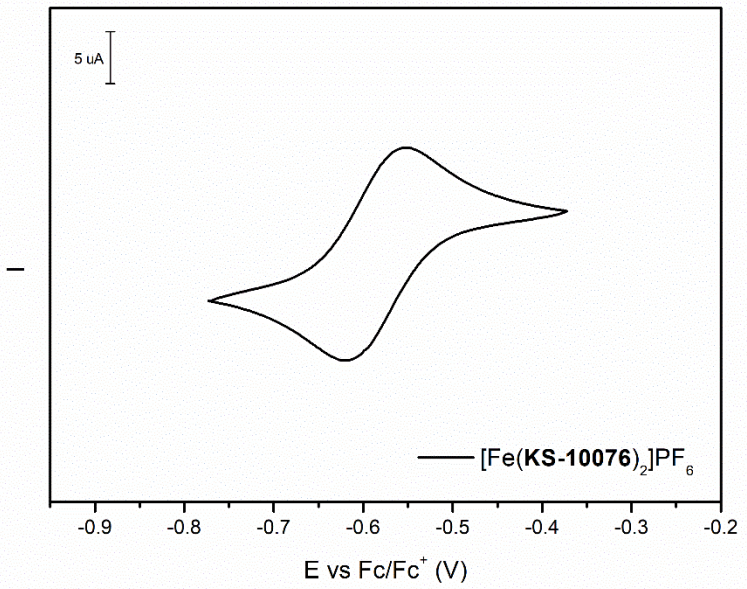

B

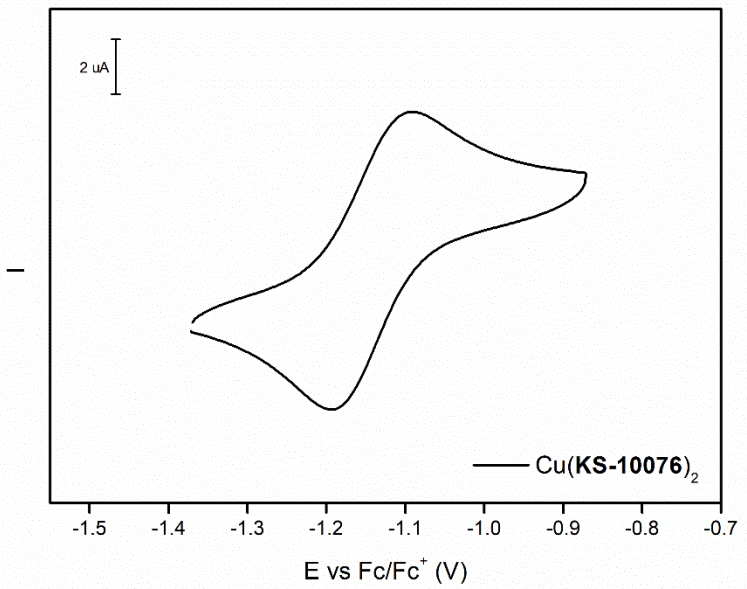

Figure S2. Cyclic voltammogram of KS10076, related to Figure 1.
(A) Cyclic voltammogram of [Fe(**KS10076**)$_2$]PF_6 (glassy carbon working electrode, 0.15 M $TBAPF_6$, scan rate 0.1 V/s in DMF, referenced to ferrocene$^{0/+}$). (B) Cyclic voltammogram of Cu(**KS10076**)$_2$ (glassy carbon working electrode, 0.15 M $TBAPF_6$, scan rate 0.1 V/s in DMF, referenced to ferrocene$^{0/+}$).

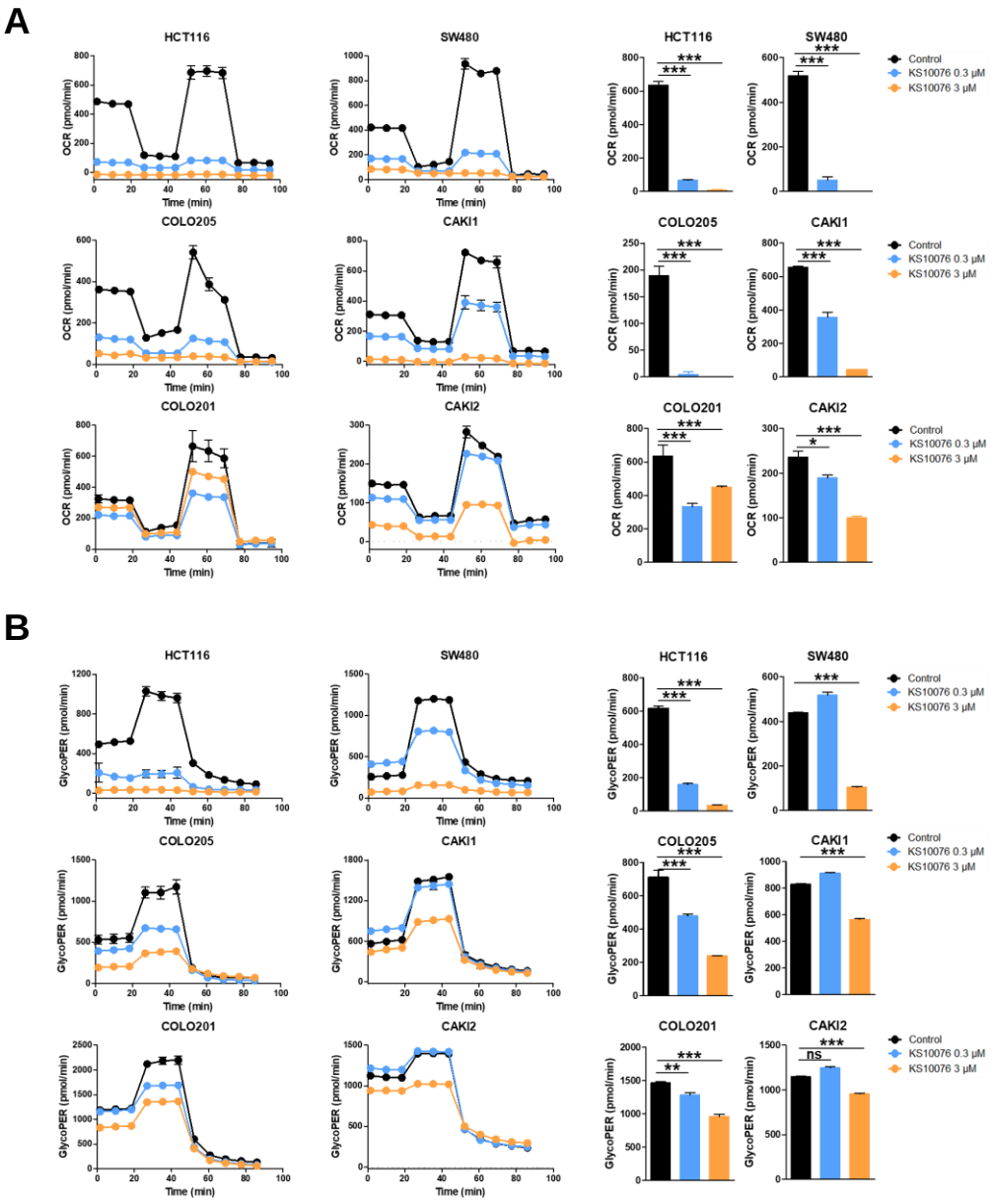

Figure S3. Metabolic profiling of KS10076 sensitive and less-sensitive cell lines, related to Figure 2

(A and B) Cells were treated with KS10076 (0.3, 3 μM) for 24 h and oxidative phosphorylation (A) and glycolysis (B) were measured. The means of triplicates are represented as data points with connecting lines. Data are presented as the mean ± SEM. * $p < 0.5$, **$p < 0.01$, and *** $p < 0.005$.

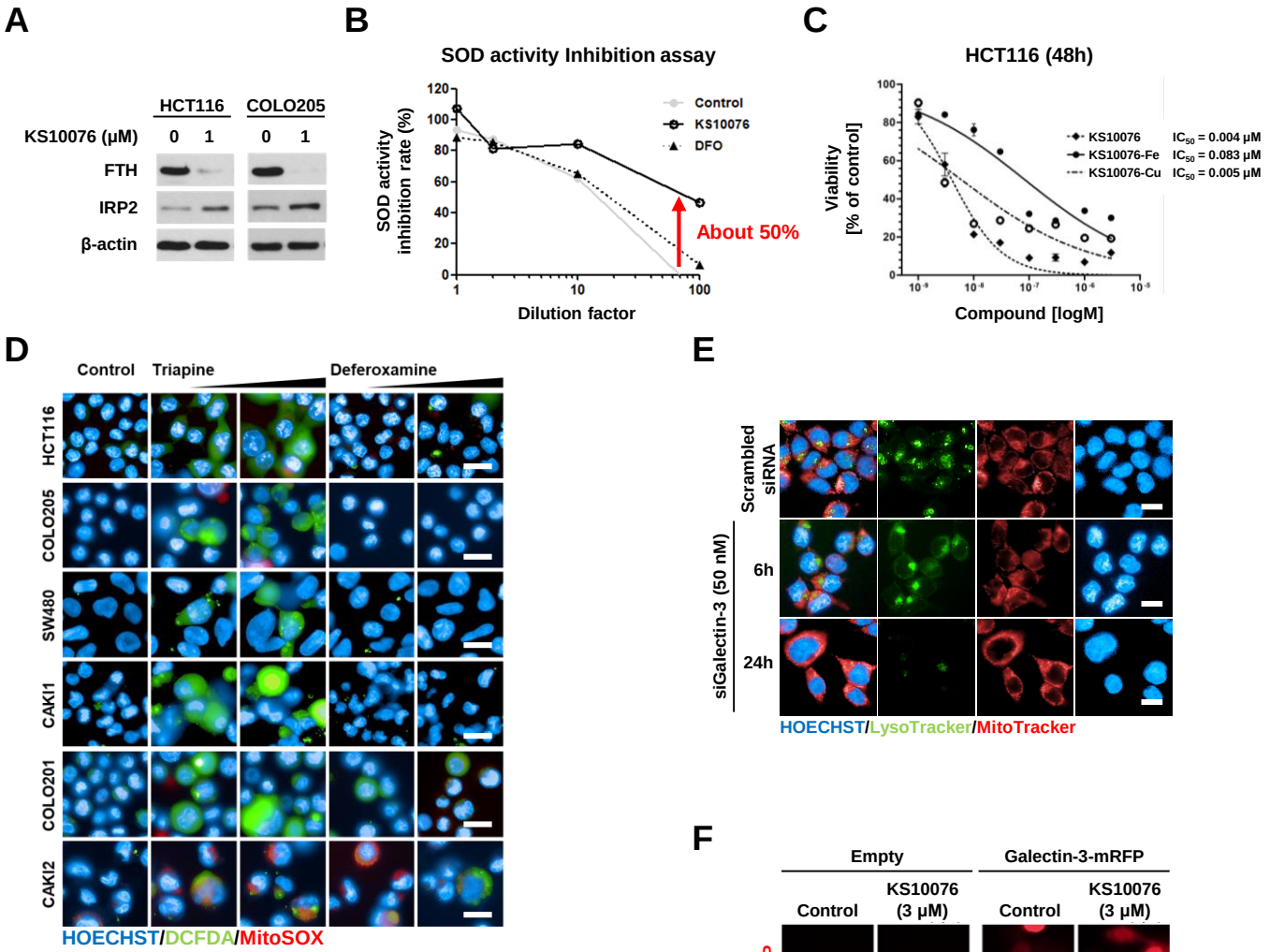

Cell line	Treatment	IC_{50} (μM) ± SEM
HCT116	KS10076	0.008 ± 0.001
	KS10076 + NAC	9.150 ± 0.584
SW480	KS10076	0.055 ± 0.002
	KS10076 + NAC	29.27 ± 0.337
LS1034	KS10076	0.074 ± 0.002
	KS10076 + NAC	6.770 ± 0.326

Figure S4. KS10076-dependent ROS generation disrupts the organelles, related to Figure 3.

(A) HCT116 and COLO205 cells were treated with KS10076 for 24 h and were subjected to immunoblotting.
(B) HCT116 cell treated with DMSO, DFO (100 μM) or KS10076 (3 μM) for 24 h was subjected for SOD inhibition assay. The means of triplicates are represented as data points with connecting lines.
(C) HCT116 cell was treated with DMSO, KS10076, [Cu]-KS10076, or [Fe]-KS10076 (at concentrations of 0 – 3 μM) for 48 h, and they were tested for growth inhibition using CCK-8 kit.
(D) Cells were treated with triapine (0.3, 3 μM) or DFO (3, 30 μM) for 24 h were subjected to ROS staining.
(E) HCT116 cell was transfected with siGalectin-3 (50 nM) for 6 or 24 h and stained with MitoTracker and LysoTracker.
(F) HCT116 cell was transfected with empty vector and galectin-3-mRFP DNA for 24 h followed by treatment of KS10076 (3 μM) and stained with LysoTracker.
(G) HCT116 cell was transfected with siCathepsin (50 nM) followed by treatment of KS10076 and subjected to cell viability assay using CCK-8 kit.
(H) HCT116, LS1034, and SW480 cells were treated with KS10076 alone or co-treated with KS10076 and NAC (5 mM) for 48 h. Two independent experiments were conducted and the table represents the mean IC_{50} with SEM. Scale bars, (D) 100 μm, (E, F) 50 μm. **$p < 0.01$.

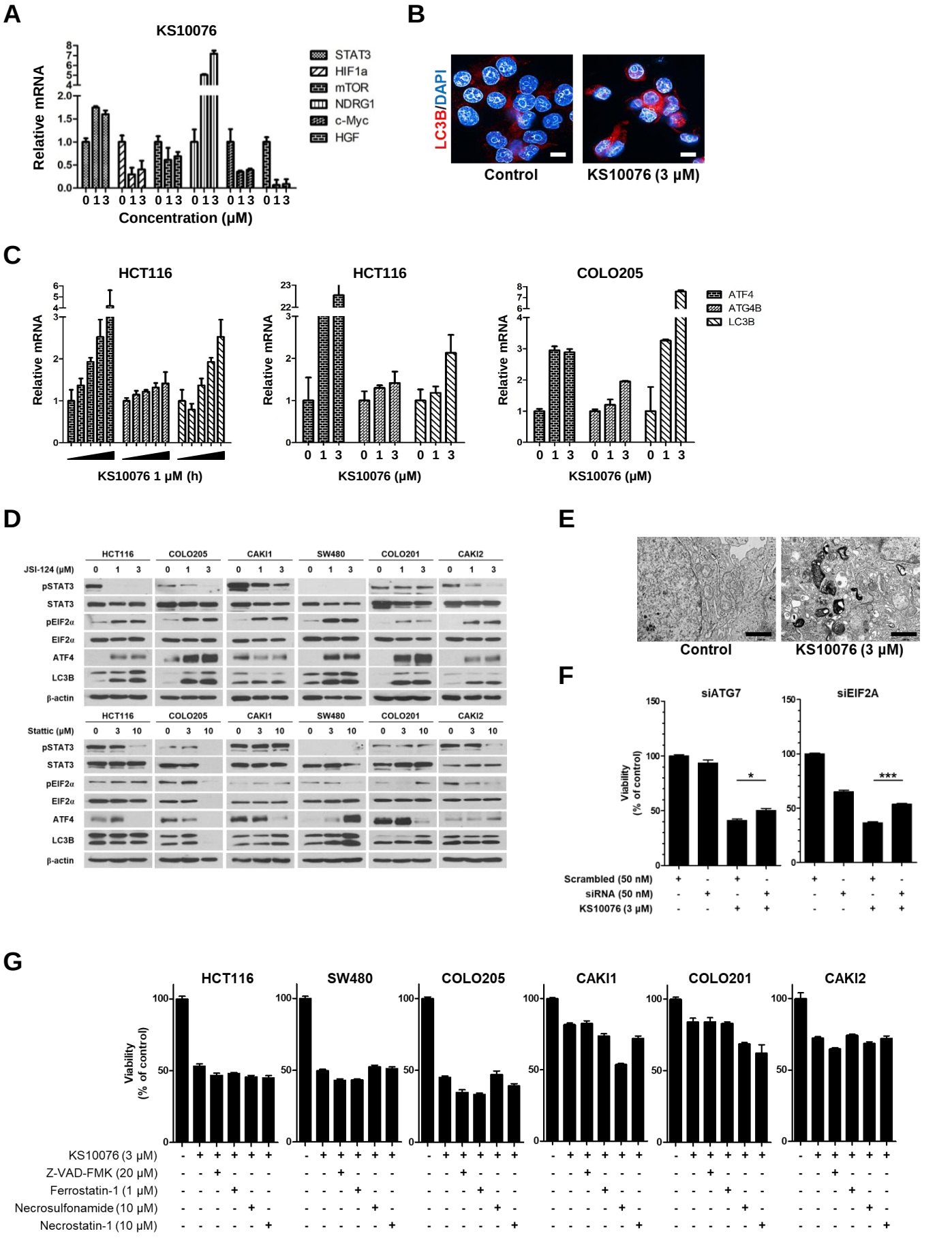
A
KS10076
Relative mRNA
STAT3
HIF1a
mTOR
NDRG1
c-Myc
HGF
0 1 3 0 1 3 0 1 3 0 1 3 0 1 3
Concentration (μM)
B
LC3B/DAPI
Control
KS10076 (3 μM)
C
HCT116
HCT116
COLO205
Relative mRNA
ATF4
ATG4B
LC3B
KS10076 1 μM (h)
KS10076 (μM)
KS10076 (μM)
D
HCT116
COLO205
CAKI1
SW480
COLO201
CAKI2
JSI-124 (μM)
Stattic (μM)
pSTAT3
STAT3
pEIF2α
EIF2α
ATF4
LC3B
β-actin
E
Control
KS10076 (3 μM)
F
siATG7
siEIF2A
Viability (% of control)
Scrambled (50 nM)
siRNA (50 nM)
KS10076 (3 μM)
G
HCT116
SW480
COLO205
CAKI1
COLO201
CAKI2
Viability (% of control)
KS10076 (3 μM)
Z-VAD-FMK (20 μM)
Ferrostatin-1 (1 μM)
Necrosulfonamide (10 μM)
Necrostatin-1 (10 μM)

Figure S5. KS10076 induces autophagic cell death independent of other cell death mechanisms, related to Figure 4.

(A) qRT–PCR results of KS10076 effect on HCT116 cells after 24 h of treatment. The results are presented as the mean ± SEM from three independent experiments.
(B) HCT116 cells were treated with KS10076 (3 μM) for 24 h and subjected to immunofluorescence staining of LC3B.
(C) qRT–PCR results of HCT116 after time-course treatment of KS10076. Also, qRT–PCR results of HCT116, LS1034, and COLO205 after 24 h treatment of KS10076 (0, 1, and 3 μM) are presented as the mean ± SEM from three independent experiments. Also, the samples were subjected to immunoblotting for protein expressions.
(D) Cells were treated with JSI-124 or Stattic for 48 h and were conducted to immunoblotting.
(E) Representative transmission electron microscopy (TEM) images of HCT116 cells treated with KS10076 for 24 h.
(F) HCT116 cell was transfected with siATG7 (50 nM) or siEIF2A (50 nM) and treated with KS10076 (3 μM). Cell viability was measured using CCK-8 kit.
(G) Cells were treated with KS10076 (3 μM) and various inhibitors of cell death for 24 h and subjected to cytotoxicity assay. Data are presented as the mean ± SEM. Scale bars, (B) 50 μm (E) 5000 nm. * $p < 0.5$ and *** $p < 0.005$.

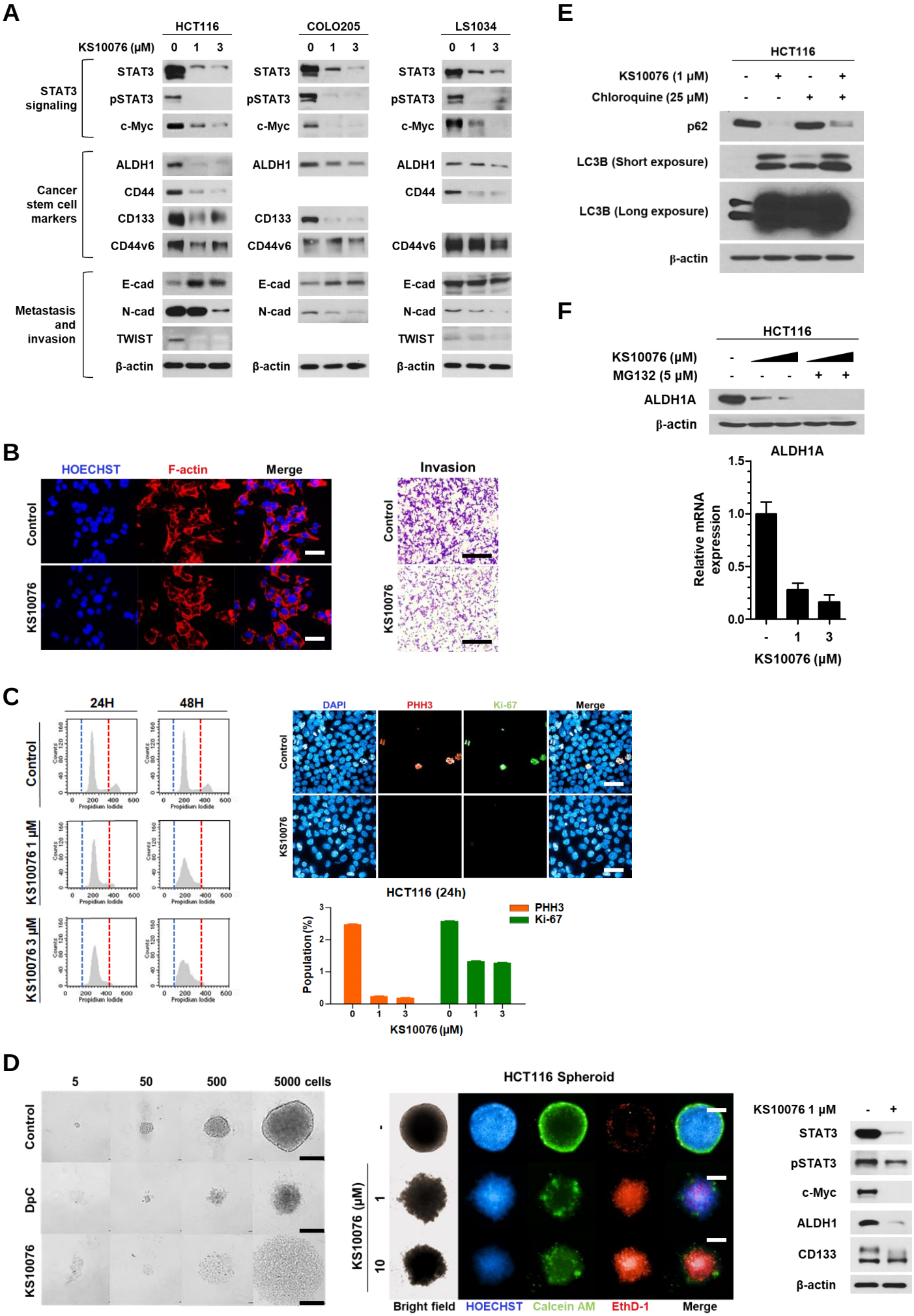
A
HCT116
COLO205
LS1034
KS10076 (μM)
0 1 3
STAT3 signaling
STAT3
pSTAT3
c-Myc
Cancer stem cell markers
ALDH1
CD44
CD133
CD44v6
Metastasis and invasion
E-cad
N-cad
TWIST
β-actin
E
HCT116
KS10076 (1 μM)
Chloroquine (25 μM)
p62
LC3B (Short exposure)
LC3B (Long exposure)
β-actin
F
HCT116
KS10076 (μM)
MG132 (5 μM)
ALDH1A
β-actin
ALDH1A
Relative mRNA expression
KS10076 (μM)
B
HOECHST
F-actin
Merge
Control
KS10076
Invasion
C
24H
48H
Propidium Iodide
KS10076 1 μM
KS10076 3 μM
DAPI
PHH3
Ki-67
Merge
HCT116 (24h)
Population (%)
KS10076 (μM)
D
5
50
500
5000 cells
Control
DpC
KS10076
HCT116 Spheroid
KS10076 (μM)
Bright field
HOECHST
Calcein AM
EthD-1
Merge
KS10076 1 μM
STAT3
pSTAT3
c-Myc
ALDH1
CD133
β-actin

Figure S6. KS10076 affects cancer cell growth, related to Figure 4 and Figure 5.
(A) HCT116, COLO205, and LS1034 cells were treated with KS10076 for 48 h and were subjected to immunoblotting for protein expression observations.
(B) HCT116 cells were treated with DMSO or KS10076 (1 μM) for 24 h, and were subjected for immunofluorescence staining and invasion assay using matrigel-coated trans-membranes.
(C) HCT116 cells were treated with DMSO or KS10076 and the cell cycle was analyzed by flow cytometry using BD FacsCalibur. Also, KS10076-treated cells were stained for immunofluorescence using cell cycle markers. The intensity of each sample was measured using normalized intensity in 6 random fields of 3 experimental replicates at 10x magnification.
(D) For tumor sphere formation assay, HCT116 cells were treated with DMSO, DPC, or KS10076 (1 μM) after seeding onto polyHEMA-coated U bottom plates. Fresh media were added every 3 days, and samples were monitored under a microscope for 10 days. On day 10, spheroids were stained using live-cell markers or subjected to immunoblotting to analyze expression of stem cell markers.
(E) HCT116 cell was treated with KS10076 (1 μM) and chloroquine (25 μM) for 24 h and subjected to immunoblotting.
(F) mRNA expression level and ALDH1 was analyzed using qRT–PCR on HCT116 cell after 24 h of KS10076 treatment (upper). Protein expression level of ALDH1 was performed using immunoblotting on HCT116 cell after 24 h of KS10076 (1, 3 μM) treatment and MG132 (5 μM) (bottom). The results are presented as the mean ± SEM from three independent experiments. (B) 100 μm (left) and 250 μm (right) (C) 100 μm (D) 250 μm (left) and 500 μm (right).

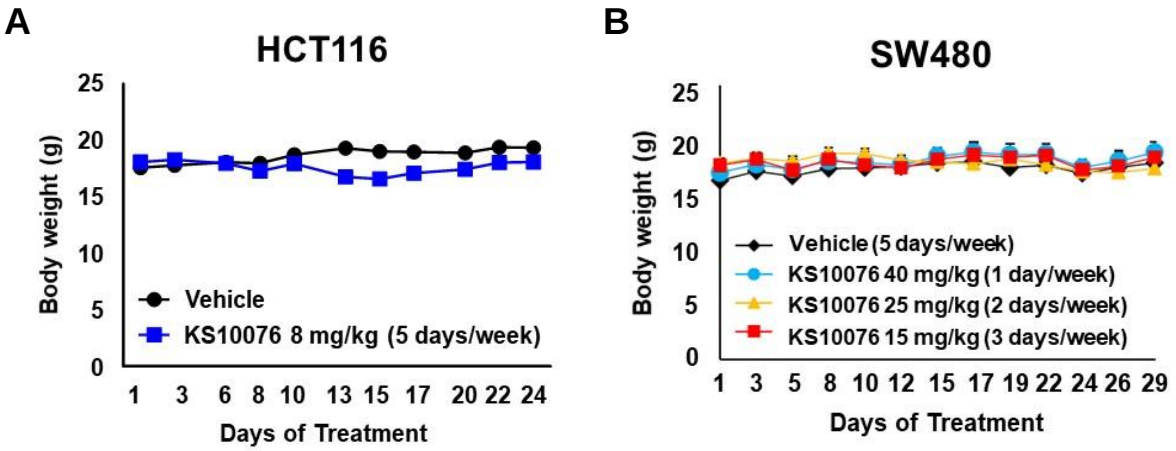

Figure S7. Body weight by administrating KS10076 of xenograft mouse, related to Figure 6.

(A) The mean body weight of HCT116 xenograft mice is represented as the data points with SD as bars.

(B) The mean body weight of SW480 xenograft mice is represented as the data points with SD as bars.

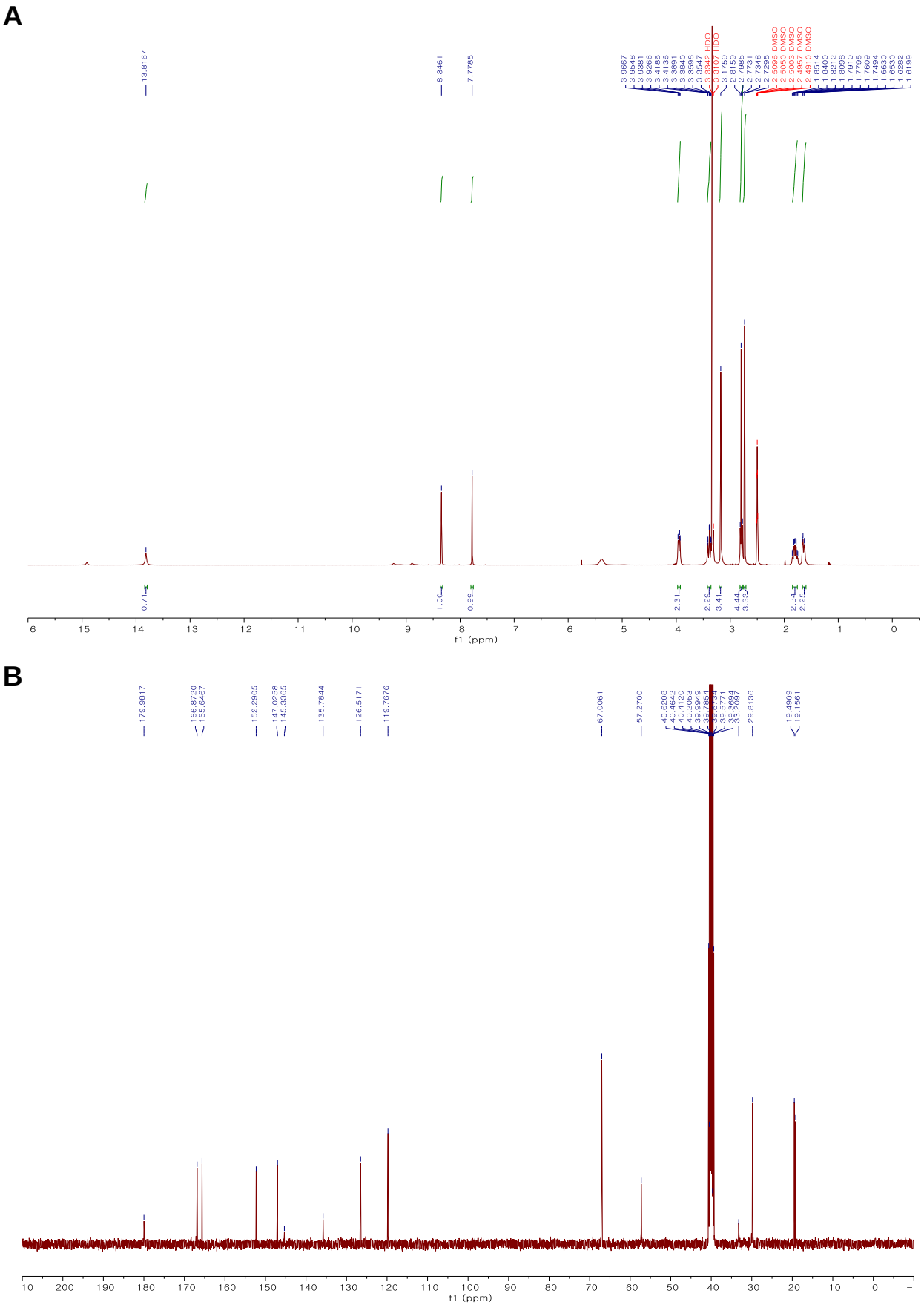

Figure S8. NMR spectrum of KS10076, Related to STAR Methods.
(A) ^{1}H NMR spectrum of KS10076 in DMSO-d_6
(B) ^{13}C NMR spectrum of KS10076 in DMSO-d_6

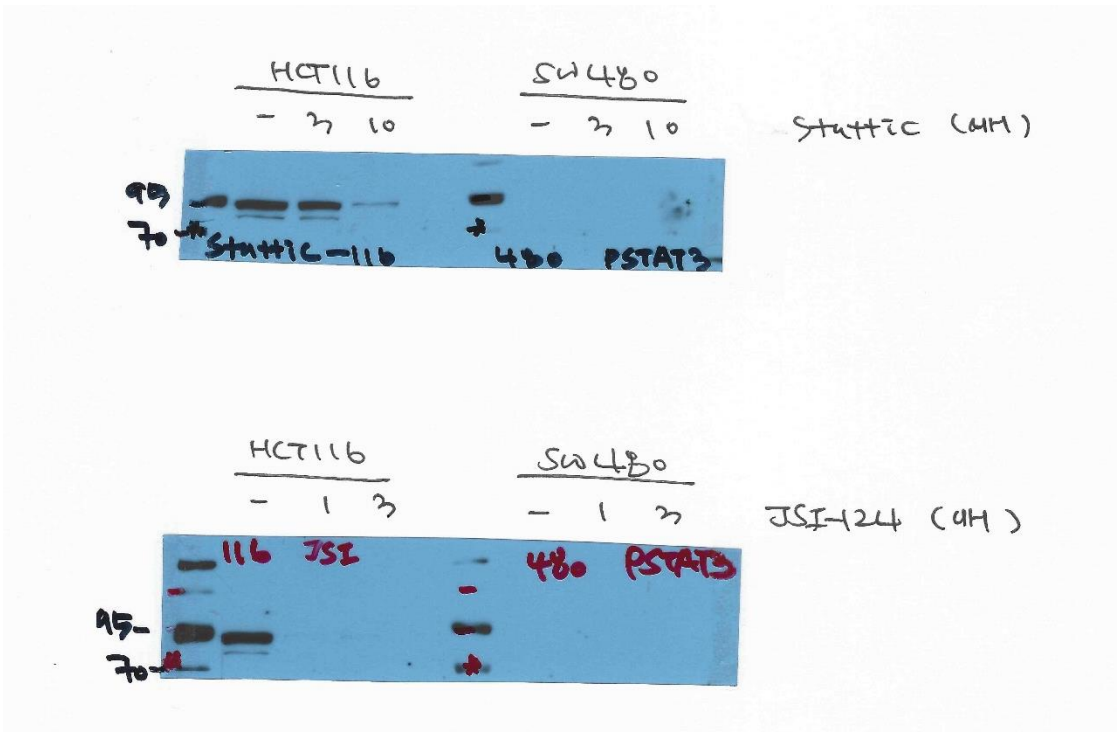

Figure S9. Original unedited blot indicating pSTAT3 (Tyr705) for representative western blots used in Figure S5D.

Table S1. Cytotoxic efficacy of KS10031 in multiple cancer cell lines, related to Figure 1.

No.	Cell line	KS10031 EC_{50} (M)	No.	Cell line	KS10031 EC_{50} (M)	No.	Cell line	KS10031 EC_{50} (M)
1	A172	8.60E-09	34	Hutu80	2.30E-09	67	NCI-H838	2.10E-08
2	A2058	1.20E-08	35	Ishikawa	2.10E-08	68	NCI-N87	2.10E-08
3	A375	6.30E-09	36	J82	4.60E-08	69	OCI-AML5	3.50E-08
4	A498	1.30E-08	37	K562	8.10E-09	70	OV56	1.80E-08
5	A549	2.50E-08	38	KARPAS299	2.10E-08	71	OVK18	1.50E-08
6	AsPC-1	2.50E-08	39	KG-1	1.40E-08	72	P31/FUJ	5.50E-08
7	BEN	4.80E-08	40	LN229	6.70E-09	73	PANC-1	1.50E-08
8	BT-20	1.30E-08	41	LNCaP	8.10E-09	74	PC3	1.50E-08
9	Caki-1	1.90E-08	42	LOU-NH91	7.60E-09	75	RERF-LC-Ad2	4.20E-09
10	Caki-2	6.70E-05	43	LOVO	1.70E-08	76	RERF-LC-MS	3.50E-08
11	Colo205	4.50E-08	44	M07e	1.90E-08	77	RKO	6.30E-09
12	COR-L279	8.60E-09	45	MCAS	2.80E-08	78	RL95-2	1.70E-08
13	COV434	2.80E-09	46	MCF-7	4.70E-09	79	RPMI8226	8.30E-09
14	DLD-1	6.80E-09	47	MDAMB231	5.60E-09	80	Saos-2 EC	4.60E-09
15	DU-145	1.00E-08	48	MDAMB435	2.60E-08	81	SCLC-21H	6.80E-09
16	DV90	1.30E-08	49	MiaPaCA2	3.90E-09	82	SJSA-1	6.10E-08
17	EFM-192A	1.10E-08	50	MKN-1	1.60E-08	83	SK-BR-3	4.30E-08
18	EFO-27	5.90E-09	51	MKN-45	1.50E-08	84	SK-ES-1	1.20E-08
19	EPLC-272H	1.30E-07	52	MOLM-13	2.00E-08	85	SK-LU-1	9.00E-08
20	H1299	1.40E-08	53	MOLT-4	7.80E-09	86	SK-MEL-3	2.20E-08
21	H4	1.20E-07	54	MV4-11	5.90E-09	87	SK-N-FI	9.30E-09
22	H460	2.70E-08	55	NCI-H1048	5.20E-09	88	SK-N-MC	3.40E-09
23	HCC1569	4.10E-07	56	NCI-H1437	1.30E-08	89	SK-N-SH	1.90E-08
24	HCC38	7.10E-08	57	NCI-H1563	8.60E-08	90	SK-OV3	1.90E-08
25	HCC827	8.30E-08	58	NCI-H1573	7.50E-07	91	SNU-1	1.10E-08
26	HCT116	1.20E-08	59	NCI-H1581	9.10E-09	92	SNU840	9.10E-09
27	HCT15	2.60E-08	60	NCI-H1703	2.80E-08	93	SW480	4.40E-09
28	HEC-1-A	1.20E-08	61	NCI-H1838	1.30E-07	94	SW620	1.40E-08
29	HEC-1-B	1.70E-08	62	NCI-H2009	7.50E-09	95	SW948	5.50E-08
30	Hep3B2.1-7	9.20E-09	63	NCI-H2110	2.80E-08	96	T84	2.80E-07
31	HL-60	1.50E-08	64	NCI-H2286	1.20E-08	97	U118MG	8.80E-08
32	HT-1080	1.20E-08	65	NCI-H292	9.10E-09	98	U2OS	1.70E-08
33	HT-29	1.20E-08	66	NCI-H441	2.40E-07	99	U87MG	1.10E-08
						100	U-937	1.10E-08

Table S2. Pharmacokinetics (PK) of metal chelators, related to Figure 1.

Compound	DpC		KS10031		KS10076	
	I.V.	P.O.	I.V.	P.O.	I.V.	P.O.
T_{max} (h)	0.120 ± 0.000	0.153 ± 0.065	0.083 ± 0.000	0.375 ± 0.144	0.083 ± 0.000	0.400 ± 0.335
C_{max} (μg/mL)	1.880 ± 0.359	1.485 ± 0.239	2.088 ± 0.670	1.648 ± 0.551	8.720 ± 5.218	5.122 ± 2.859
$T_{1/2}$ (h)	3.996 ± 1.152	5.682 ± 1.813	15.98 ± 6.378	16.35 ± 2.264	22.29 ± 9.287	46.11 ± 17.52
$AUC_{0\text{-}8\ hr}$ (μg·h/mL)	5.377 ± 1.803	5.219 ± 1.201	13.74 ± 4.438	19.01 ± 5.783	58.06 ± 9.659	86.94 ± 17.52
AUC_{inf} (μg·h/mL)	7.487 ± 2.222	9.800 ± 3.264	21.46 ± 8.234	28.91 ± 7.809	72.38 ± 8.527	171.1 ± 74.56
CL (mL/h/kg)	287.2 ± 91.55		110.1 ± 60.05		27.88 ± 3.152	
V_{SS} (mL/kg)	1724 ± 594.2		2077 ± 616.5		785.7 ± 374.3	
*BA (%)		38.82 ± 8.93		55.34 ± 16.83		171.1 ± 74.56
		DpC	KS10031	KS10076		
Plasma protein binding rate (%)	Mouse	99.98 ± 0.01	99.92 ± 0.00	99.86 ± 0.02		
	Rat	98.87 ± 0.82	98.68 ± 1.15	95.12 ± 4.48		
	Human	99.54 ± 0.39	99.61 ± 0.08	98.80 ± 0.34		
Plasma stability (%)	Mouse	70.17 ± 4.20	84.74 ± 3.90	84.69 ± 7.44		
	Rat	59.89 ± 10.66	86.95 ± 5.48	73.27 ± 2.01		
	Human	50.21 ± 2.69	59.47 ± 5.09	76.08 ± 5.09		

Table S4. The cancer organoids characteristics derived from individual CRC patient, related to Figure 5.

	YCO001	YCO004	YCO006	YCO007	YCO009	YCO011	YCO012	YCO013	YCO016	YCO019
ICDO*	Transverse colon	Rectum, NOS	Hepatic flexure of colon	Ascending colon	Ascending colon/ Sigmoid colon	Rectum, NOS	Rectum, NOS	Rectum, NOS	Sigmoid colon	Ascending colon
EGFR	Focal and moderate staining (2+)	None	None	None	Negative (0)	Weakly positive in tumor cells	None	Focal and moderate staining (2+)	None	None
BRAF	Wild	None	None	None	None	None	None	Wild	None	None
KRAS mutation	Wild	KRAS G12D	Wild	Wild	Wild	KRAS G12D	Wild	KRAS G13D	Wild	KRAS G13D
Microsatellite instability	MSS	MSI-High	MSI-High	MSS	MSS	MSS	MSS	MSS	MSI-High	MSS
5-FU IC_{50} (μM)	21.3	22	10.6	83.2	25.1	19.3	17	>130	>130	129.5
KS10076 IC_{50} (nM)	428	90	300	895	790	178	811	475	21	15